Author/s:
Van Koeverden, MP;Abrahams, BF;Hua, C;Hudson, TA;Robson, R

Title:
Inducing Structural Diversity in Anionic Metal-Tetraoxolene Coordination Polymers Using Templating Methyl Viologen Countercations

Date:
2022-02-02

Citation:
Van Koeverden, M. P., Abrahams, B. F., Hua, C., Hudson, T. A. & Robson, R. (2022). Inducing Structural Diversity in Anionic Metal-Tetraoxolene Coordination Polymers Using Templating Methyl Viologen Countercations. Crystal Growth and Design, 22 (2), pp.1319-1332. https://doi.org/10.1021/acs.cgd.1c01277.

Persistent Link:
https://hdl.handle.net/11343/324303

Inducing Structural Diversity in Anionic Metal–Tetraoxolene Coordination Polymers Using Templating Methyl Viologen Countercations

Martin P. van Koeverden†, Brendan F. Abrahams, Carol Hua‡, Timothy A. Hudson, Richard Robson.*

School of Chemistry, The University of Melbourne, Parkville, VIC 3010, Australia.

† Present Address: School of Chemistry, The University of Sydney, Sydney, NSW 2006, Australia.

‡ Present Address: School of Life and Environmental Sciences, Deakin University, Waurn Ponds, VIC 3216, Australia

*Email: bfa@unimelb.edu.au

chloranilate, fluoranilate, topology, viologens, coordination polymers.

Abstract

Controlling the connectivity of coordination polymers is an important scientific goal, as the physicochemical properties of these compounds are often intimately linked to the network topology. Using redox-active methyl viologen (MeV^{2+}) countercations, a series of one-, two- and three-dimensional anionic coordination polymers are described in which Mn^{II} or Cd^{II} centers are bridged with tetraoxolene ligands derived from 3,6-dihalo-2,5-dihydroxy-1,4-benzoquinone (H_2Xan, X = F, Cl). Using MeV^{2+} countercations and either Mn^{II} or Cd^{II}, yields non-porous anionic diamond networks of general composition $(MeV)[M(Clan)_2]$, in which 8-coordinate divalent metal centers are linked by $Clan^{2-}$ ligands. Changing the solvent mixture from acetone/water to acetonitrile/water ($MeCN/H_2O$) affords the same product in the case of Cd^{II}, but for Mn^{II} an anionic 2D honeycomb network with composition $(MeV)[Mn_2(Clan)_3]\cdot 6MeCN$ is obtained. In contrast, the use of Fan^{2-} ligands affords 1D ladder-type anionic coordination polymers $(MeV)[M_2(Fan)_3(H_2O)_2]$ (M = Mn^{II}, Cd^{II}), despite the chemical and structural similarity of Fan^{2-} and $Clan^{2-}$ ligands. In the case of the diamond and 2D networks, MeV^{2+} countercations play a key structural role, arising from C–H···O hydrogen bonding extending from the cation to the anionic network. For the 1D ladder-type structures formed with Fan^{2-}, O–H···O hydrogen bonding between anionic $[M_2(Fan)_3(H_2O)_2]^{2-}$ ladders is largely responsible for directing crystal packing. For these compounds, MeV^{2+} cations play a more nuanced structural role, only occupying void space between layers of H-bonded anionic $[M_2(Fan)_3(H_2O)_2]^{2-}$ ladders.

INTRODUCTION

Crystalline coordination polymers and metal-organic frameworks (MOFs) have shown significant promise for application in gas storage and separation,[1-3] reaction catalysis,[4, 5] sensing,[6, 7] and as porous magnetic[8-10] and electrically conductive materials.[11-13] The potential to tailor the structure, porosity, and functionality of coordination polymers, through judicious selection of constituent metals and ligands, represents a key advantage compared to traditional inorganic materials. Although many properties such as electrochemical reversibility, magnetic ordering and catalytic activity are directly linked to the identity of the constituent metals and ligands, the coordination polymer topology can also have a considerable effect upon the material's properties. Most obvious is the major impact topology has upon pore geometry and surface area, however long-range magnetic ordering and electrical conductivity are also particularly sensitive to the network connectivity.

The effect of topology on physical properties is exemplified in by the series of magnetic anionic bimetallic oxalate $[M^{II}M^{III}(ox)_3]^-$ (M^{II} = Mn, Fe, Co, Ni, Cu, Zn; M^{III} = Cr, Fe; ox^{2-} = oxalate) networks. The topology of the networks is readily varied by changing the charge-balancing countercations.[14, 15] Alkylammonium countercations afford 2D layered (6,3) honeycomb (**hex**) networks,[16, 17] whereas the bulkier $[Z^{II}(2,2'\text{-bpy})_3]^{2+}$ (Z = Fe, Co, Ni, Ru; 2,2′-bpy = 2,2′-bipyridine) or $[Z^{III}Cp^*_2]^+$ (Z = Fe, Co; Cp^* = pentamethylcyclopentadienyl) cations help template chiral 3D (10,3)-*a* (**srs**) networks.[18-20] Although the 2D and 3D networks have equivalent $[M^{II}M^{III}(ox)_3]^-$ network formulations and therefore metal coordination environments, spontaneous magnetic ordering typically occurs at markedly higher temperatures in the 2D layered networks (up to T_c = 48 K for $(^nHx_4N)[Fe^{II}Fe^{III}(ox)_3]$, $^nHx_4N^+$ = tetra-*n*-hexylammonium)[17] compared to the 3D networks (T_c = 6.6 K for $[Fe^{II}(2,2'\text{-bpy})_3][Co^{II}Cr^{III}(ox)_3](ClO_4)$).[20] This disparity is ascribed to different

alignments of the magnetic anisotropy axes between the 2D and 3D materials,[21] thereby demonstrating the importance of controlling network topology to obtain materials with desirable physical properties.

Tetraoxolene ligands derived from 2,5-dihydroxy-1,4-benzoquinone (H_2dhbq) and the 3,6-disubstituted analogues (termed anilic acids, H_2Xan, X = F, Cl, Br, I, CN, NO_2 etc.) have been widely used to synthesize a variety of coordination polymers,[15, 22-28] and also possess properties that allow the generation of porous electrically conductive and magnetic materials.[15] Tetraoxolenes can exist in three common redox states when coordinated to metal centers: the dianionic quinonoid form ($dhbq^{2-}$ or Xan^{2-}); a paramagnetic semiquinonoid trianion ($dhbq^{3-\bullet}$ or $Xan^{3-\bullet}$); and an aromatic tetraanion ($dhbq^{4-}$ or Xan^{4-}) state (Scheme 1).[29-31] The semiquinonoid $dhbq^{3-\bullet}$ or $Xan^{3-\bullet}$ states mediates strong magnetic exchange between paramagnetic metal centers,[30] in contrast to the closed shell $dhbq^{2-}$/Xan^{2-} and $dhbq^{4-}$/Xan^{4-} forms.[29, 31] Therefore materials which contain the $dhbq^{3-\bullet}$ or $Xan^{3-\bullet}$ forms can exhibit spontaneous magnetic ordering[32-37] or single-chain magnetism.[38, 39] In addition, tetraoxolene coordination polymers with intrinsic mixed valency, due to the presence of both $dhbq^{2-}$/Xan^{2-} and $dhbq^{3-\bullet}$/$Xan^{3-\bullet}$ redox states, are electrically conductive because intervalence charge transfer (IVCT) between the different ligand valence states provides a pathway for long-range charge transport.[32, 34, 40-44]

Scheme 1. Redox states of the tetraoxolene ligands (X = H, F, Cl, Br, I, CN, NO_2 etc.) (upper) and structure of the *N*,*N*′-dimethyl-4,4′-bipyridinium (methyl viologen, MeV^{2+}) cation (lower).

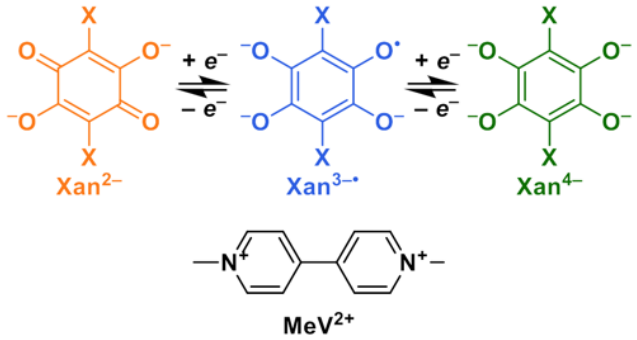

Myriad tetraoxolene coordination polymers have been synthesized including: 1D linear strips,[45, 46] zig-zag,[27, 39] crankshaft,[47] and ladder-like chains;[48] 2D neutral[26, 28, 49-53] and anionic sheets;[23, 24, 33, 36, 38, 40, 52, 54-60] and 3D neutral and anionic networks.[28, 41, 43, 52, 61-63] Despite the structural diversity of tetraoxolene coordination polymers, the 2D (6,3) honeycomb (**hex**) and 3D (10,3)-*a* (**srs**) topologies still predominate amongst anionic tetraoxolene coordination polymers where *d*-block metal centers serve as 3-connecting nodes.[15, 52] The size, shape and charge of countercations play a key structure directing role with respect to the network topology and geometry adopted by anionic tetraoxolene coordination polymers.[15, 52, 54, 59-61] As expected, N–H···O hydrogen bonds extending from alkylammonium cations e.g. $Et_2NH_2^+$ or $Me_2NH_2^+$, to O atoms of the tetraoxolene ligands have a considerable effect on the resulting structure.[64, 65] Although C–H···O hydrogen bonds extending from alkylammonium cations, e.g. Me_4N^+ or Et_4N^+, are significantly weaker, they are also capable of impacting on the overall structure.[59, 60]

Functional and/or redox-active cations have remarkably been seldom used as countercations for anionic metal–tetraoxolene compounds,[66-70] so the ability of such cations to influence the structure and properties of tetraoxolene coordination polymers is largely unknown. Quaternized bipyridinium cations, termed viologens, are a particularly interesting class of functional cation,[71] that have been widely incorporated into a range of materials such as electrochromics[72, 73] and

molecular switches.[74, 75] This stems largely from the tunable redox activity of viologens,[76, 77] and their ability to engage in supramolecular heterophilic charge-transfer interactions with π-electron rich species,[78, 79] and homophilic radical-radical interactions.[80, 81] We recently introduced an approach using viologen-like redox-active countercations to guide assembly of a mixed-valence Fe–tetraoxolene coordination polymer.[34] In this case, the close face-to-face association of the electron-deficient viologen countercation with the anionic tetraoxolene network caused partial localization of the electron-rich semiquinonoid $Clan^{3-\bullet}$ state of the ligand in the anionic network. This behavior contrasts with mixed-valence Fe–tetraoxolene frameworks using redox-inactive alkylammonium countercations, which typically exhibit complete delocalization of the Xan^{2-} and $Xan^{3-\bullet}$ states.[32, 33, 41-43, 59] . Herein, we report a further exploration of the structural effect that redox-active *N*,*N*′-dimethyl-4,4′-bipyridinium (methyl viologen, MeV^{2+}, Scheme 1) cations exert on anionic tetraoxolene coordination polymers involving Mn and Cd metal centers.

RESULTS AND DISCUSSION

The Mn^{II} and Cd^{II} framework materials were synthesized by carefully layering aqueous solutions of metal nitrate, methyl viologen ditosylate ($MeV(OTs)_2$) and $LiOAc{\cdot}2H_2O$, below organic solvent solutions of the reduced forms of fluor- or chloranilic acid, 3,6-difluoro-1,2,4,5-tetrahydroxybenzene (H_4Fan) and 3,6-dichloro-1,2,4,5-tetrahydroxybenzene (H_4Clan) respectively. Crystals appeared on the vial walls in addition to the vial bottom within two days, which were harvested after seven days. Employing a similar synthetic approach used in our previous work,[34, 59, 61] involving slow aerial oxidation of H_4Xan to the active H_2Xan form under slow diffusion conditions, a crystalline product suitable for single crystal X-ray diffraction (SC-XRD) was produced. In the case of the chloranilate-based coordination polymers both 2D and 3D

networks were obtained. In contrast, the fluoranilate-based products are exclusively 1D coordination polymers. The formation of the various compounds described in this report is indicated in Scheme 2.

Scheme 2. Metal-tetraoxolene coordination polymers formed in the presence of methyl viologen

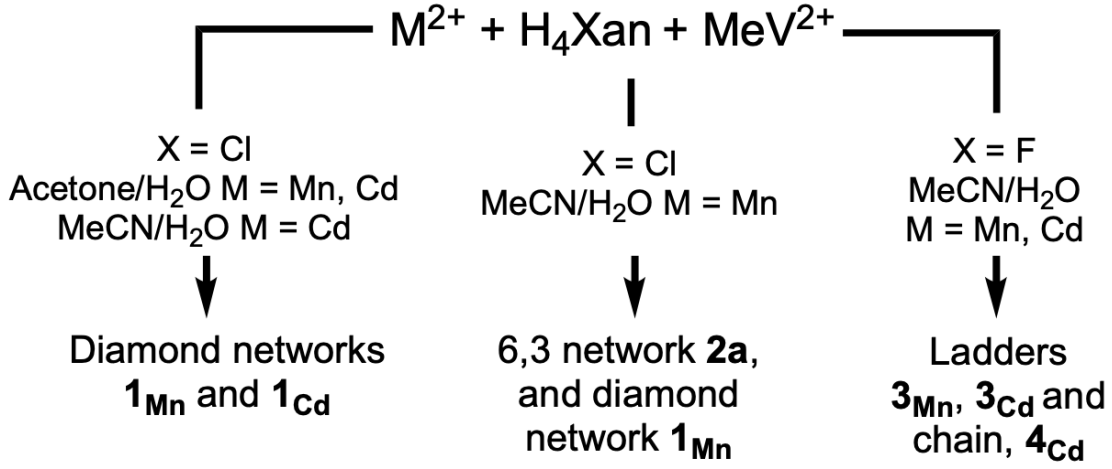

Chloranilate Coordination Polymers

An aqueous solution of $MeV(OTs)_2$ and $Mn^{II}(NO_3)_2{\cdot}4H_2O$ layered below an acetone solution of H_4Clan, yielded bright red elongated octahedra of composition $(MeV)[Mn(Clan)_2]$ (**1**$_{Mn}$). The use of $Cd^{II}(NO_3)_2{\cdot}4H_2O$ in place of $Mn^{II}(NO_3)_2{\cdot}4H_2O$ afforded the isostructural diamagnetic analogue $(MeV)[Cd(Clan)_2]$ (**1**$_{Cd}$). The compound **1**$_{Cd}$, could also be obtained when an MeCN–H_2O solvent system was employed, but the same solvent mixture failed to yield **1**$_{Mn}$, producing instead crystals of composition $(MeV)[Mn_2(Clan)_3]{\cdot}6MeCN$ (**2a**). The unpredictable effect of solvent on the course of the reaction, under otherwise equivalent reaction conditions, highlights the delicately balanced nature of the supramolecular interactions which govern coordination polymer assembly.

The structures of **1**$_{Mn}$ and **1**$_{Cd}$ were determined by single-crystal X-ray diffraction (SC-XRD) (Table S1), with the crystalline phase purity of bulk samples of **1**$_{Mn}$ and **1**$_{Cd}$ (synthesized using either acetone–H_2O or MeCN–H_2O solvent systems) determined by P-XRD analysis (Figure S1 &

S2). The solvent-free nature of $\mathbf{1}_{\mathbf{Mn}}$ and $\mathbf{1}_{\mathbf{Cd}}$ was confirmed by a combination of FT-IR spectroscopy (Figure S3) and elemental analyses. Thermogravimetric analyses (TGA) confirmed the absence of solvent and also revealed that each of the network materials remained thermally stable until a temperature of 300 °C (Figure S4).

A satisfactory structure solution and refinement was obtained for compounds $\mathbf{1}_{\mathbf{Mn}}$ and $\mathbf{1}_{\mathbf{Cd}}$ in the orthorhombic space group, *Fddd*. The asymmetric unit consists of a $Clan^{2-}$ ligand residing on an inversion center, and a divalent metal center and a charge-balancing MeV^{2+} cation. Both the metal center and methyl viologen are located on sites of 222 symmetry. The C–O and diagnostic C–C ligand bond lengths in both $\mathbf{1}_{\mathbf{Mn}}$ and $\mathbf{1}_{\mathbf{Cd}}$ are consistent with the expected quinonoid $Clan^{2-}$ form of the ligand (see SI for detailed analysis of bond distances). Similarly, analysis of the C–C and C–N bond for the MeV^{2+} moieties in $\mathbf{1}_{\mathbf{Mn}}$ and $\mathbf{1}_{\mathbf{Cd}}$ compared to known structures of MeV^{2+},[82, 83] and $MeV^{+\bullet}$,[80, 84] supports assignment of the aromatic dicationic oxidation state of MeV^{2+} (Figure S6 and Table S3, see ESI for extended discussion).

Each Mn^{II} center in $\mathbf{1}_{\mathbf{Mn}}$ is coordinated by four crystallographically equivalent, chelating $Clan^{2-}$ ligands (Figure 1a) and adopts a slightly distorted triangular dodecahedral coordination geometry as indicated by calculation of the Continuous Shape Measure (CShM) parameter[85, 86] (Table S2). The chelation of each of the $Clan^{2-}$ ligands is asymmetric with Mn–O distances of 2.1674(12) and 2.4869(12) Å. The Mn^{II} center lies 0.679(4) Å away from the plane of the 6-membered ring of each $Clan^{2-}$ ligand. A similar asymmetric chelation geometry is apparent in $\mathbf{1}_{\mathbf{Cd}}$, although not to the same extent as in $\mathbf{1}_{\mathbf{Mn}}$ ($d_{Cd–O}$ = 2.273(2) and 2.512(2) Å). The coordination geometry in $\mathbf{1}_{\mathbf{Cd}}$ is closer to that of a perfect triangular dodecahedron (Table S2), with the Cd^{II} centers residing 0.738(5) Å outside the mean plane of the 6-membered ring of the $Clan^{2-}$ ligand.

Each metal ion in $\mathbf{1}_{\mathbf{Mn}}$ and $\mathbf{1}_{\mathbf{Cd}}$ acts as a 4-connecting node in a 3D diamond (**dia**) network, by linking to four symmetry-related metal centers through bridging $Clan^{2-}$ ligands. A representation of the adamantane-type unit in the $[Mn(Clan)_2]^{2-}$ network is presented in Figure 1b. While the diamondoid topology is amongst the most prevalent 3D topologies exhibited by coordination polymers and metal-organic frameworks (MOFs),[87-89] 3D diamondoid metal–tetraoxolene frameworks are relatively rare. To date, diamondoid tetraoxolene networks have only been observed using (pseudo)lanthanoid (Y^{III}, Ho^{III}, Ce^{III} or Er^{III}),[28, 52, 62] actinoid (Th^{IV})[28] or post-transition metal (Bi^{III})[90] centers. In $\mathbf{1}_{\mathbf{Mn}}$ and $\mathbf{1}_{\mathbf{Cd}}$, the relatively large ionic radii of Mn^{II} and Cd^{II} (0.97 Å and 1.09 Å respectively) allows for the accommodation of four $Clan^{2-}$ around each metal center.

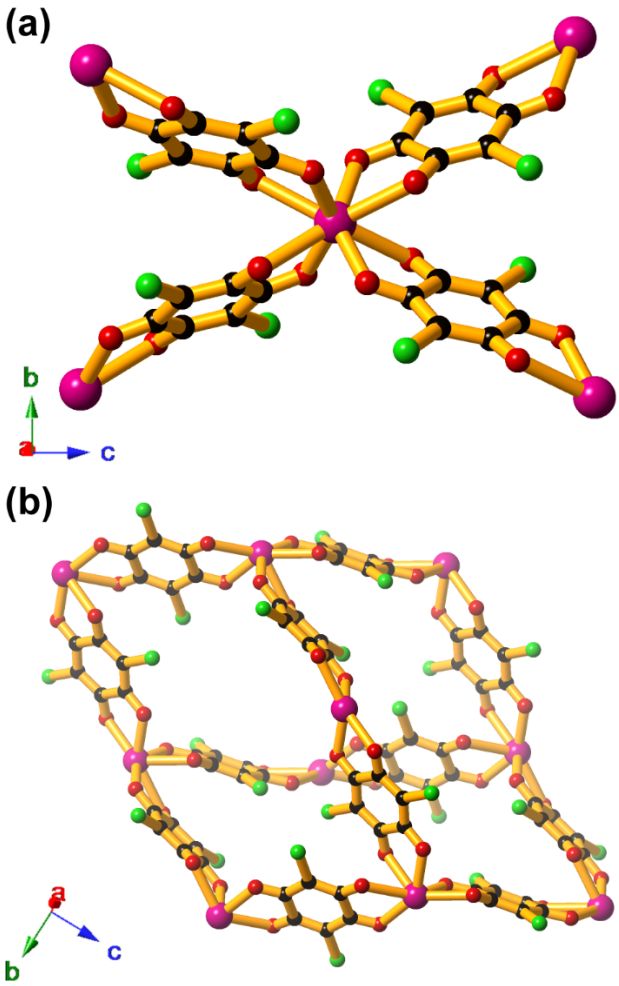

Figure 1. (a) The 8-coordinate environment around Mn nodes in $\mathbf{1_{Mn}}$. (b) Ball-and-stick representation of the adamantane unit of the $[Mn(Clan)_2]^{2-}$ network in $\mathbf{1_{Mn}}$. Magenta = Mn, green = Cl, red = O, and black = C.

A charge-balancing, MeV^{2+} cation resides at the center of the adamantane-type unit, with the long axis of the cation oriented parallel to the crystallographic *c* axis (Figure 2a & Figure S7). The cation is distorted from planarity with the two aromatic rings rotated relative to each other around the central C–C bond. The anionic $[Mn(Clan)_2]^{2-}$ network forms a close embrace around the MeV^{2+} countercations (Figure 2b) involving multiple C–H···O interactions. The most significant contacts occur between the pyridinium rings of MeV^{2+} and the O donor atoms of the $Clan^{2-}$ ligands (Figure 2c; $d_{H\cdots O}$ = 2.555–2.758 Å for $\mathbf{1_{Mn}}$ and $d_{H\cdots O}$ = 2.530–2.652 Å for $\mathbf{1_{Cd}}$; a summary is provided in Table S7). These interactions appear to be responsible for relative rotation of the pyridinium rings around the central C–C bond of MeV^{2+} moieties (39.4° for $\mathbf{1_{Mn}}$ and 39.7° for $\mathbf{1_{Cd}}$), and for the close contact between the Cl atom of $Clan^{2-}$ with the π-system of the MeV^{2+} ($d_{Cl\cdots\pi}$ = 3.386 Å for $\mathbf{1_{Mn}}$ and 3.439 Å for $\mathbf{1_{Cd}}$).

The shape and size of the MeV^{2+} cation, and its strong electrostatic attraction for the anionic network is likely to be responsible for the distortion from the ideal diamond network. In $\mathbf{1_{Mn}}$, the Mn···Mn separation across bridging $Clan^{2-}$ ligands is 8.356 Å. For an ideal diamond net with regular tetrahedral centers separated by 8.356 Å, the dimensions of the adamantane unit (and cell dimensions), would be 19.297 × 19.297 × 19.297 Å, with a corresponding cell volume of 7186 $Å^3$. The dimensions of the adamantane unit of $\mathbf{1_{Mn}}$, defined by orthogonal Mn···Mn separations, match those of the orthorhombic unit cell of $\mathbf{1_{Mn}}$ i.e. 18.041 × 10.061 × 26.277 Å, with a 34% reduction

in cell volume from the ideal value, to 4770 Å^3. The contraction of the idealized *b* axis length from *ca.* 19.3 to 10.1 Å is likely to result from the attraction between the anionic network and the approximately rod-shaped MeV^{2+} cation. This strong electrostatic attraction between the network and the MeV^{2+} cations brings C–H groups from MeV^{2+} into close proximity with O atoms of the network, leading to multiple C–H···O interactions (Figure 2c) and producing a relatively dense, non-porous crystal. The long separation of 26.277 Å corresponds to the distance across the adamantane unit coinciding with the long axis of the MeV^{2+} (Figure 2a). In the case of $\mathbf{1}_{\mathbf{Cd}}$ a corresponding cell volume reduction from 7643 to 4870 Å^3 represents a decrease of 36%. Each MeV^{2+} cation also protrudes slightly through the chair-like conformation windows into adjacent adamantane voids (Figure 2d), producing a relatively dense, non-porous crystal. The location and interactions of MeV^{2+} in $\mathbf{1}_{\mathbf{Mn}}$ and $\mathbf{1}_{\mathbf{Cd}}$ contrasts with our previous work, in which a viologen-like 1,10-phenanthroline-derived dication engaged with strong Coulombic and charge-transfer interactions with π-electron rich $Clan^{3-\bullet}$ ligands in a mixed-valence Fe–chloranilate framework.[34]

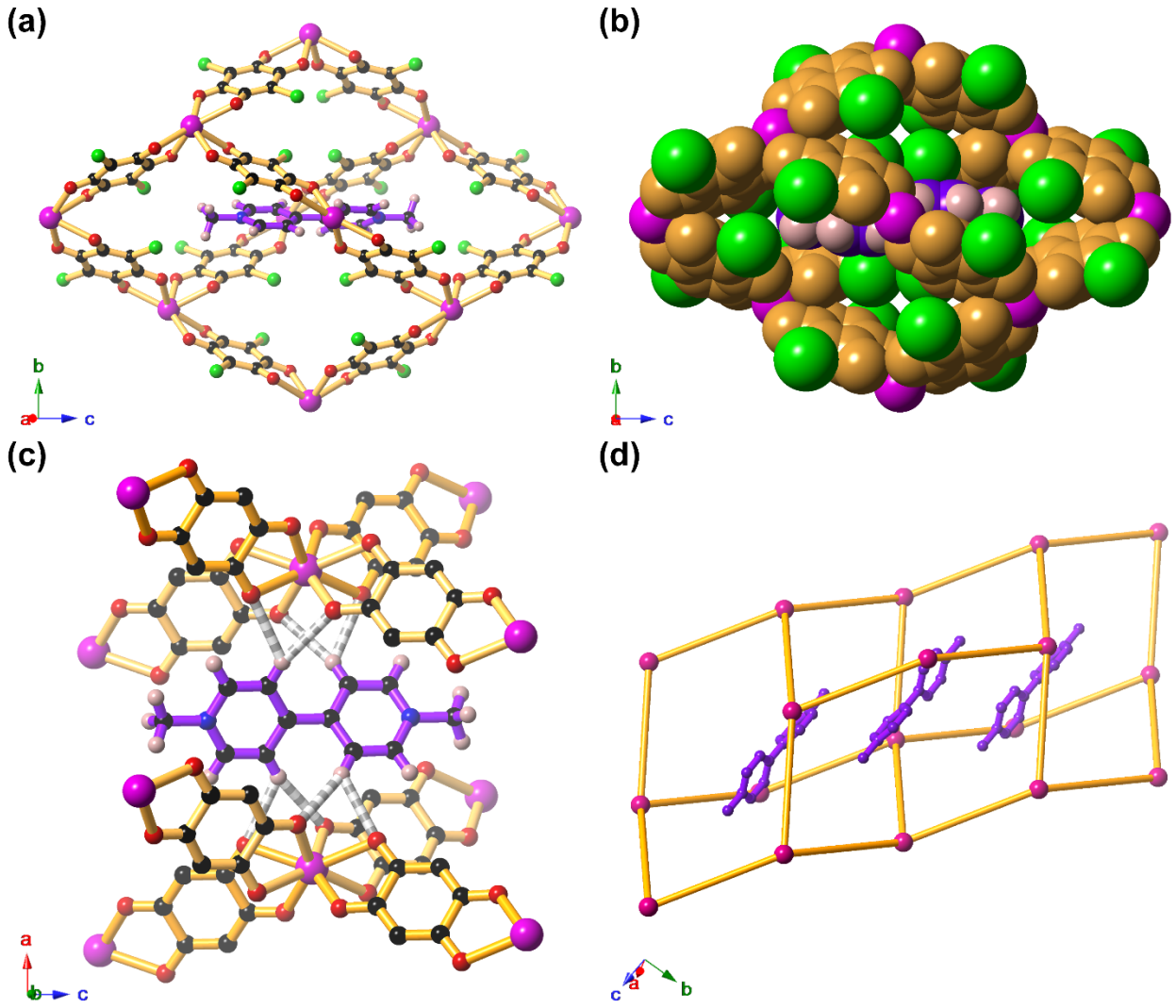

Figure 2. (a) Ball-and-stick and (b) spacefilling representations of the interactions between MeV^{2+} cations (purple) and the anionic $[Mn(Clan)_2]^{2-}$ network of $\mathbf{1}_{Mn}$ (tan). (c) C–H···O interactions (dash grey) between MeV^{2+} (purple) and the anionic $[Mn(Clan)_2]^{2-}$ network (tan). Cl atoms omitted for clarity. (d) Packing of the MeV^{2+} cations (purple) within the adamantane voids of the diamondoid $[Mn(Clan)_2]^{2-}$ network of $\mathbf{1}_{Mn}$. Only the topological representation of the anionic $[Mn(Clan)_2]^{2-}$ network (tan) is shown for clarity. Magenta = Mn, green = Cl, red = O, blue = N, black = C, and pale pink = H.

In contrast to $\mathbf{1_{Cd}}$, which can be synthesized using either acetone–H_2O or MeCN–H_2O solvent systems, a reaction involving $Mn^{II}(NO_3)_2$, $MeV(OTs)_2$ and H_4Clan with an MeCN–H_2O solvent system yields reddish-brown plates of the 2D coordination polymer $(MeV)[Mn_2(Clan)_3]\cdot 6MeCN$ (**2a**). Structure determination using SC-XRD indicated the triclinic *P*−1 space group (Table S5). P-XRD analysis conducted on an MeCN slurry of **2a** (to preserve the solvation state) shows good agreement between the experimental pattern and that predicted from SC-XRD analysis (Figure S8); the slight mismatch in lattice parameters is ascribed to thermal expansion of the unit cell, noting the differing temperatures used between SC-XRD and P-XRD measurements. The asymmetric unit of **2a** includes one Mn^{II} center and three well-ordered MeCN molecules, each located on general positions. In addition, the asymmetric unit contains three inequivalent $Clan^{2-}$ ligands ($\mathbf{L_1}$, $\mathbf{L_2}$ and $\mathbf{L_3}$) and a charge-balancing MeV^{2+} cation, each of which is located on a center of inversion, giving a contribution of one half each in the asymmetric unit. The presence of well-ordered MeCN molecules in the crystal structure suggests this solvent plays a role in templating the structure. The Mn^{II} centers adopt a slightly distorted octahedral coordination environment formed by six O donor atoms of bridging bis-bidentate $Clan^{2-}$ ligands. The mean $d_{Mn–O}$ = 2.174(1) Å is consistent with Mn^{II} while the mean ligand $d_{C–O}$ (1.256(1), 1.256(1) and 1.258(1) Å for $\mathbf{L_1}$, $\mathbf{L_2}$ and $\mathbf{L_3}$ respectively) and $d_{C–C}$ (1.541(2), 1.541(2) and 1.537(2) Å for $\mathbf{L_1}$, $\mathbf{L_2}$ and $\mathbf{L_3}$ respectively) values indicate the $Clan^{2-}$ valence state, as was the case in the diamond networks described above. Comparing the $d_{C–C}$ and $d_{C–N}$ values between the MeV^{2+} moieties in **2a**, and MeV^{2+} and $MeV^{+\bullet}$ structures reported in literature (Figure S6 and Table S4), supports assignment of the MeV^{2+} valence state in **2a**.

The structure of **2a** consists of anionic 2D $[Mn_2(Clan)_3]^{2-}$ sheets in which 3-connecting Mn^{II} centers are linked *via* bis-bidentate $Clan^{2-}$ ligands. Each Mn^{II} center, of either Δ or Λ configuration,

links to three other Mn^{II} centers of the opposite configuration, affording a $[Mn_2(Clan)_3]^{2-}$ honeycomb (6,3) (**hex**) network (Figure 3a). The $[Mn_2(Clan)_3]^{2-}$ sheets, which lie parallel to the crystallographic (111) plane, stack upon each other with a separation between mean planes of 7.033 Å (Figure 3b). Compared to trigonally symmetric (6,3) networks for which alkylammonium cations serve as counterions e.g. $(Cat)_2[M_2(Xan)_3]$ (M = Zn, Mn, Fe; X = F, Cl; Cat = Me_4N^+, Et_4N^+),[36, 42, 59] the Mn···Mn···Mn angles in the anionic sheets of **2a** are significantly distorted from 120°, to 115.09°, 130.20° and 114.46°. The distorted 2D network is likely due to the interactions between MeV^{2+} cations and the anionic $[Mn_2(Clan)_3]^{2-}$ network.

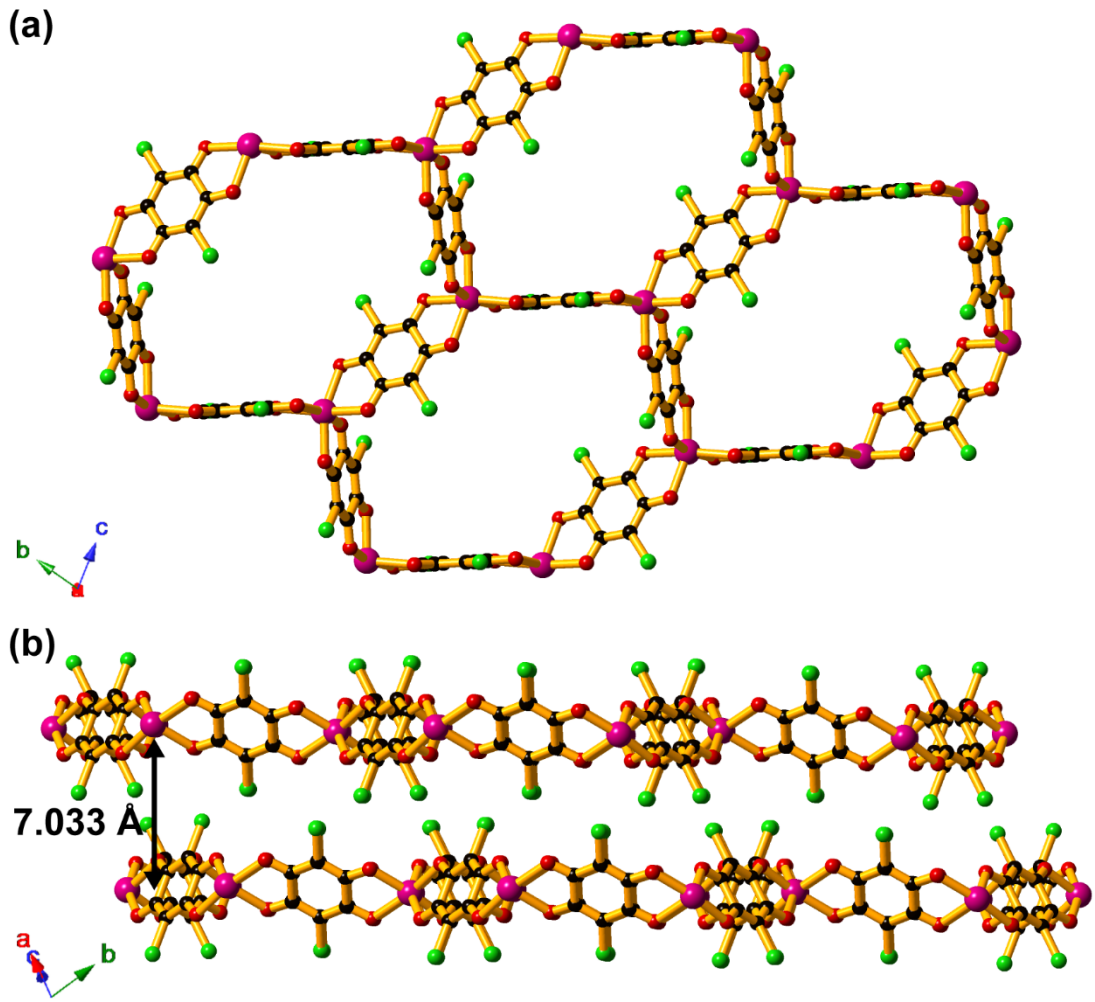

Figure 3. The anionic (6,3) honeycomb $[Mn_2(Clan)_3]^{2-}$ sheets in **2a** viewed along (a) the crystallographic *a* axis, and (b) the plane of the anionic sheets parallel to the crystallographic (111) plane. Magneta = Mn, green = Cl, red = O, and black = C.

Each MeV^{2+} cation is neatly sandwiched between two $\mathbf{L_1}$ $Clan^{2-}$ ligands from anionic sheets above and below (Figure 4a & b, Figure S9). This arrangement produces an alternating stacking motif of $Clan^{2-}$ and MeV^{2+} species when viewed along the crystallographic *a* axis (Figure 4c). This cation–network packing arrangement is similar to that observed in (PhenQ)$[Fe_2(Clan)_3]$·solvent ($PhenQ^{2+}$ = 5,6-dihydropyrazino[1,2,3,4-*lmn*][1,10]-phenanthrolindiium), in which viologen-like $PhenQ^{2+}$ cations are closely packed between the $[Fe_2(Clan)_3]^{2-}$ layers.[34] In contrast, both MeV^{2+} and $Clan^{2-}$ are electron-deficient so charge-transfer (CT) interactions are probably not a significant driving force for cation packing. The coplanar conformation and position of MeV^{2+} cations between the anionic sheets likely arises from C–H···O interatomic contacts between the cations and the $[Mn_2(Clan)_3]^{2-}$ sheets above and below each cation. The H3, H3′, H5 and H5′ atoms of MeV^{2+} (H22 and H24 in the crystal structure) form a pincer which engages in close C–H···O interactions ($d_{H\cdots O}$ = 2.381 and 2.405 Å) with O donor atoms of $\mathbf{L_3}$ in anionic sheets above and below each cation (Figure 4d). Steric interactions between Cl atoms of $\mathbf{L_3}$ in sheets above and below, and the face of the MeV^{2+} cations also act to fence the MeV^{2+} to its location between the $[Mn_2(Clan)_3]^{2-}$ sheets where it adopts a planar conformation. The MeV^{2+} cation, which is located on a center of inversion, causes the Mn coordination spheres linked by the C–H···O bonding to have opposite configurations. The transmission of stereochemical information through the MeV^{2+} cations leads to long-range ordering of Mn^{II} configurations between layers.

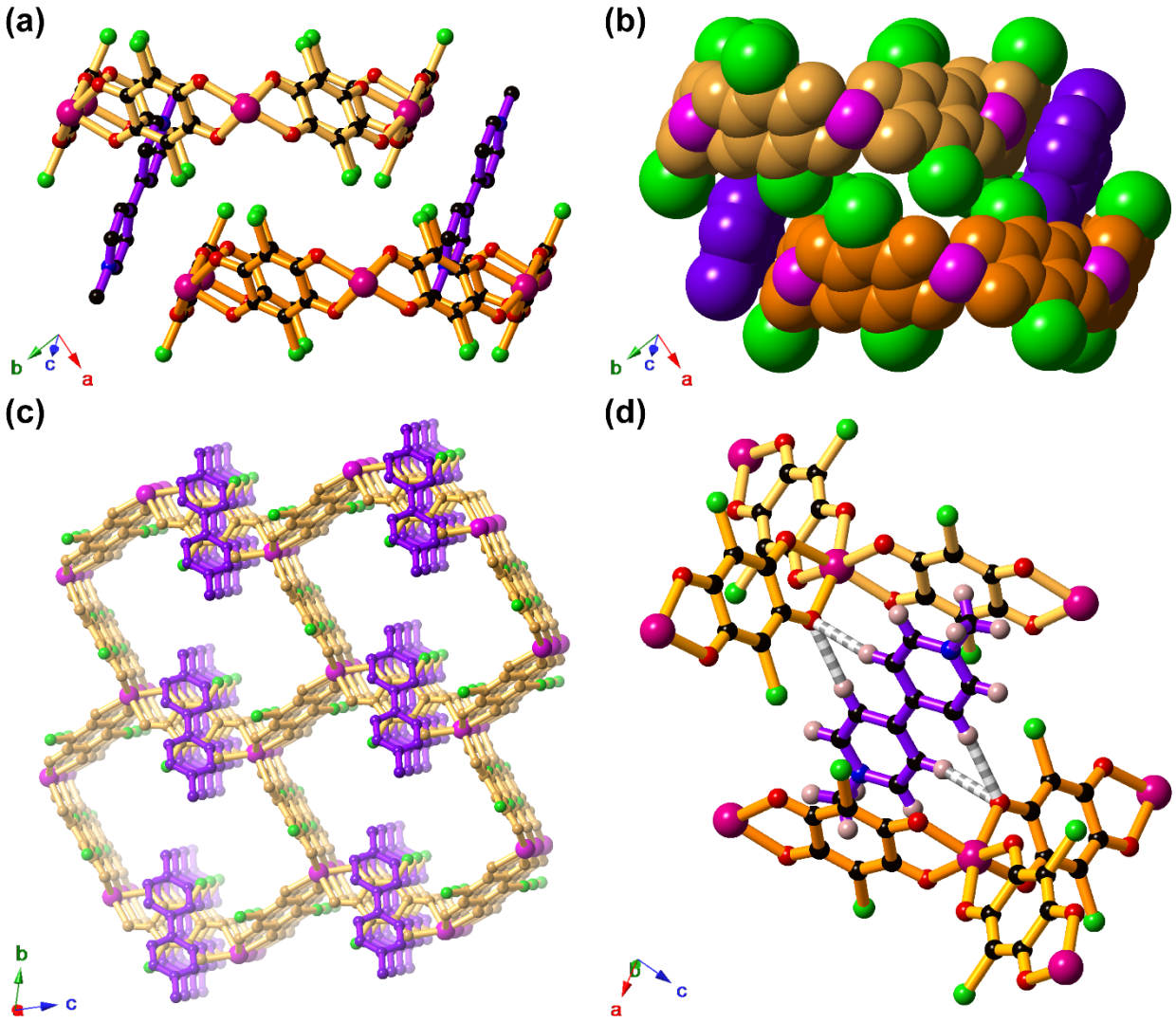

Figure 4. (a) Ball-and-stick and (b) spacefilling representations of the interactions between MeV^{2+} cations (purple) with the $[Mn_2(Clan)_3]^{2-}$ sheets above (tan) and below (orange) in **2a**. (c) View along crystallographic *a* axis showing alternating stacking motif of MeV^{2+} (purple) with $Clan^{2-}$ ligands in the anionic $[Mn_2(Clan)_3]^{2-}$ sheets (tan). (d) C–H···O interactions (dashed grey) between MeV^{2+} (purple) and the anionic $[Mn_2(Clan)_3]^{2-}$ sheets above (tan) and below (orange). Magenta = Mn, green = Cl, red = O, blue = N, black = C. H atoms and ordered MeCN in channels not shown for clarity.

Although P-XRD analysis on a slurry of the bulk product suggests **2a** is the dominant crystalline phase (Figure S8), optical microscopy of the crystalline product reveals the presence of a small quantity of bright red octahedra of similar habit to $\mathbf{1_{Mn}}$. Measurement of the cell parameters of one of these crystals confirmed these crystals are the $\mathbf{1_{Mn}}$ phase. Despite numerous attempts using varied reaction conditions, co-crystallization of a small quantity of $\mathbf{1_{Mn}}$ with **2a** could not be avoided. As described previously, an analogous reaction using $Cd^{II}(NO_3)_2$ and an MeCN–H_2O solvent system leads to crystallization of only the $\mathbf{1_{Cd}}$ phase, instead of a hypothetical (MeV)[Cd_2(Clan)$_3$]·6MeCN compound. These results suggest that the templating role of MeCN in affording the honeycomb sheet structure is probably quite weak. Moreover, co-crystallization of the $\mathbf{1_{Mn}}$ and **2a** phases possibly reflects slight differences in the kinetic and thermodynamic stability of each phase, which favors exclusively the 3D **dia** phase in the case of Cd^{II}. The presence of $\mathbf{1_{Mn}}$ in the bulk product is more clearly apparent in P-XRD analysis upon isolation of the crystalline product from the solvent. P-XRD analysis of the isolated solid shows only reflections attributable to the 3D **dia** phase $\mathbf{1_{Mn}}$ (Figure S10), consistent with **2a** losing crystallinity upon loss of MeCN from the structure, to form a non-crystalline product which we refer to as **2b**. The transformation of **2a** to **2b** is possibly driven by H_2O from atmospheric moisture replacing MeCN during isolation of **2b**, as evinced by FT-IR spectroscopy and TGA. The ATR FT-IR spectrum of **2b** exhibits a strong, broad absorbance at 3300 cm^{-1} attributed to H_2O (Figure S11a), which is absent in the spectrum of $\mathbf{1_{Mn}}$ (Figure S3). Additionally, TGA upon **2b** show two distinct mass losses below 200 °C (Figure S11b), whereas $\mathbf{1_{Mn}}$ shows no mass loss to 350 °C (Figure S4a), as it contains no lattice solvent molecules.

Fluoranilate Coordination Polymers

Slow diffusion of MeCN solutions of H_4Fan into aqueous solutions of $Mn^{II}(NO_3)_2$ or $Cd^{II}(NO_3)_2$, and $MeV(OTs)_2$ yields isostructural 1D ladder-like compounds $(MeV)[Mn_2(Fan)_3(H_2O)_2]\cdot y MeCN\cdot z H_2O$ ($\mathbf{3_{Mn}}$) and $(MeV)[Cd_2(Fan)_3(H_2O)_2]\cdot y MeCN\cdot z H_2O$ ($\mathbf{3_{Cd}}$). For both compounds, satisfactory structure refinements were obtained in the triclinic space group, *P*–1 (Table S6). The structure description below mainly refers to the archetype, $\mathbf{3_{Mn}}$. The asymmetric unit of $\mathbf{3_{Mn}}$ contains two crystallographically independent metal centers (Mn1 and Mn2), and four unique Fan^{2-} ligands ($\mathbf{L_1}$ through $\mathbf{L_4}$). Both $\mathbf{L_1}$ and $\mathbf{L_3}$ reside on sites of –1 symmetry, whereas $\mathbf{L_2}$ and $\mathbf{L_4}$ are located on general positions. Additionally, the asymmetric unit contains a charge-balancing MeV^{2+} cation and two H_2O molecules, each coordinated to Mn1 and Mn2. A combination of ordered and disordered H_2O and MeCN solvent molecules complete the asymmetric unit. The mean $d_{M–O}$ values of 2.181(11) and 2.179(11) Å for Mn1 and Mn2 respectively are consistent with Mn^{II}. In the case of $\mathbf{3_{Cd}}$ the Cd–O distances are typical for Cd^{II} with average values of 2.285(1) and 2.282(9) Å for Cd1 and Cd2 respectively. As for the chloranilate compounds, comparison of the mean ligand $d_{C–O}$ and characteristic $d_{C–C}$ bond lengths in $\mathbf{3_{Mn}}$ and $\mathbf{3_{Cd}}$ to those in known Fan^{2-} compounds,[43, 59] confirms $\mathbf{L_1}$ through to $\mathbf{L_4}$ exist in the expected oxidized quinonoid Fan^{2-} state. Analogously, comparison of the $d_{C–C}$ and $d_{C–N}$ values for MeV^{2+} in $\mathbf{3_{Mn}}$ and $\mathbf{3_{Cd}}$ confirm the expected dicationic MeV^{2+} state (Figure S6 & Table S4), allowing the $\mathbf{3_{Mn}}$ and $\mathbf{3_{Cd}}$ to be formulated with $(MeV^{2+})[M^{II}_2(Fan^{2-})_3(H_2O)_2]$ charge state distributions.

The repeating polymeric unit of $\mathbf{3_{Mn}}$ consists of four Mn^{II} centers arranged in a $Mn_4(Fan)_4$ parallelogram. Two parallel edges of the $Mn_4(Fan)_4$ unit are formed by the bridging bis-bidendate Fan^{2-} ligands $\mathbf{L_1}$ and $\mathbf{L_3}$, while the two other parallel edges comprise bridging Fan^{2-} $\mathbf{L_2}$ and $\mathbf{L_4}$ ligands which are bidentate at one end, and monodendate at the other (Figure 5a). The slightly distorted octahedral coordination environment of the Mn^{II} centers is therefore formed from five O

donor atoms from the Fan^{2-} ligands, with the remaining coordination site occupied by a molecule of H_2O. Within the structure of $\mathbf{3_{Mn}}$, one ordered MeCN molecule occupies the $Mn_4(Fan)_4$ cavity (Figure 5b). The snug fit of the MeCN suggests that rod-like molecule plays a templating role in generating of the $Mn_4(Fan)_4$ unit. The 1D ladders in $\mathbf{3_{Mn}}$ are formed from edge-sharing $Mn_4(Fan)_4$ units, with the long axis of the 1D $[M_2(Fan)_3(H_2O)_2]^{2-}$ ladders oriented parallel to the (1 –1 0) plane (Figure 5c); bridging bis-bidentate $\mathbf{L_1}$ and $\mathbf{L_3}$ form the rungs of the ladder, while bridging $\mathbf{L_2}$ and $\mathbf{L_4}$ ligands form the ladder side rails. Similar structural features are apparent in $\mathbf{3_{Cd}}$ although the MeCN molecule occupying the $Cd_4(Fan)_4$ unit exhibits a small degree of disorder.

Considering the chemical and structural similarity between fluor- and chloranilic acid, the disparate structures of $\mathbf{3_{Mn}}$ and $\mathbf{3_{Cd}}$ compared to **2a** is surprising given the equivalent metal to ligand stoichiometry. In our experience metal–fluoranilate coordination polymers typically only exhibit slight structural disparities compared to their metal–chloranilate analogues,[42, 43, 59] with Fan^{2-} and $Clan^{2-}$ ligands in the structures existing in the same coordination modes.

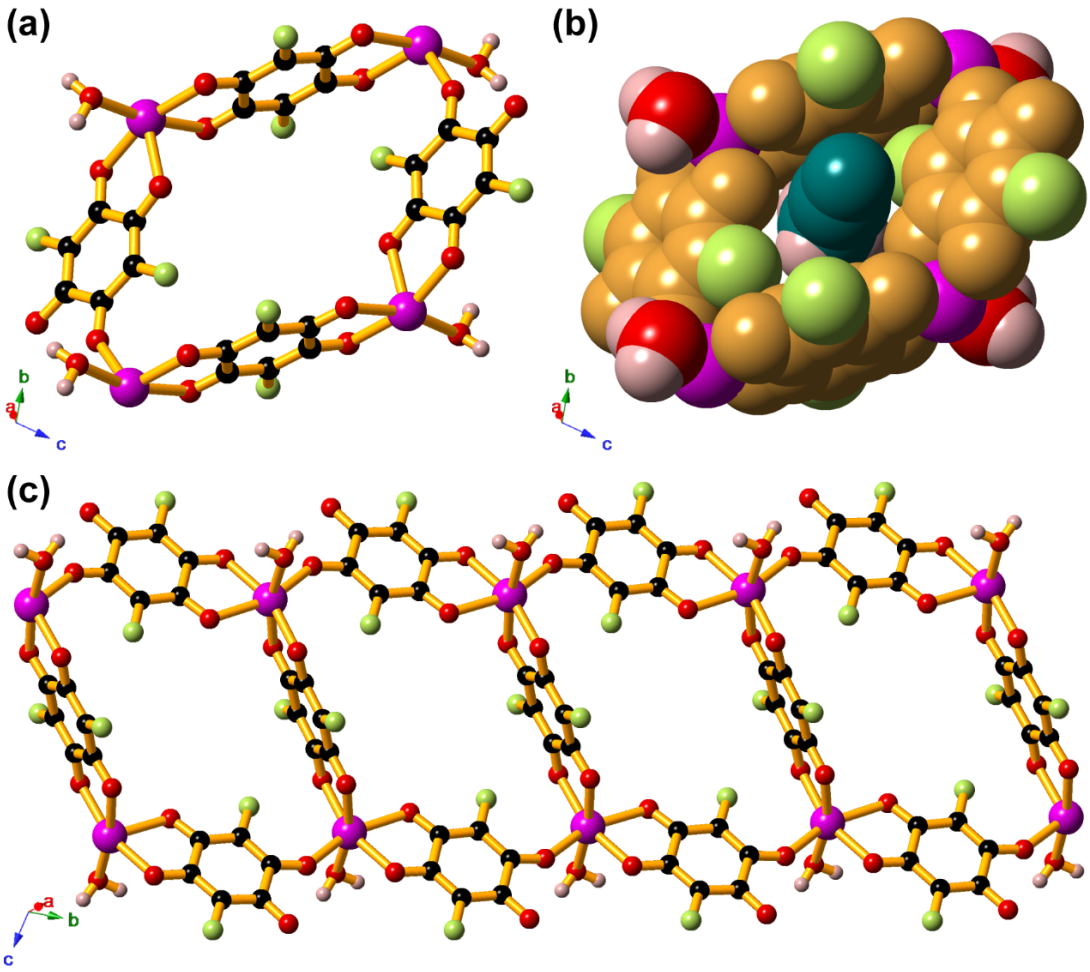

Figure 5. (a) Coordination environment around Mn^{II} centers in $\mathbf{3}_{\mathbf{Mn}}$, forming $Mn_4(Fan)_4$ parallelograms. (b) Templating role of MeCN (teal) upon the $Mn_4(Fan)_4$ parallelogram (tan). (c) Anionic $[Mn_2(Fan)_3(H_2O)_2]^{2-}$ ladders formed by edge-sharing $Mn_4(Fan)_4$ parallelograms in $\mathbf{3}_{\mathbf{Mn}}$. Magenta = Mn, pale green = F, red = O, black = C, pale pink = H.

Molčanov and coworkers observed a similar 1D ladder motif and crystal packing in the compound $(2,2'\text{-bpyH}^+)_2[Mn_2(Clan)_3(H_2O)_2]\cdot 2H_2O$,[48] though there are notable differences to both $\mathbf{3}_{\mathbf{Mn}}$ and $\mathbf{3}_{\mathbf{Cd}}$. The $Mn_4(Fan)_4$ parallelograms in $\mathbf{3}_{\mathbf{Mn}}$ and $\mathbf{3}_{\mathbf{Cd}}$ are sheared to a greater extent along the direction of the ladder axis, so the M···M···M angles (70.3° and 109.7 ° for $\mathbf{3}_{\mathbf{Mn}}$; 67.5° and 112.4°

for $\mathbf{3_{Cd}}$) differ notably from those in (2,2′-bpyH$^+$)$_2$[Mn$_2$(Clan)$_3$(H$_2$O)$_2$]·2H$_2$O (80.4° and 99.6°). These differences presumably arise from the smaller van der Waals radius of F compared to Cl, which allows closer contact between adjacent Fan^{2-} ligands, as indicated by C–F···C contacts ($d_{F\cdots C}$ = 2.980(3) and 2.988(3) Å in $\mathbf{3_{Mn}}$; $d_{F\cdots C}$ = 2.992(3) and 3.022(3) Å in $\mathbf{3_{Cd}}$), compared to the equivalent C–Cl···C contacts ($d_{Cl\cdots C}$ 3.402(3) Å) in (2,2′-bpyH$^+$)$_2$[Mn$_2$(Clan)$_3$(H$_2$O)$_2$]·2H$_2$O.[48]

The differences in electronic structure between various coordination modes of tetraoxolene ligands give rise to differences in vibration stretching frequencies,[91-93] allowing the presence of bis-bidentate ($\mathbf{L_1}$ and $\mathbf{L_3}$) and mono and bidentate ($\mathbf{L_2}$ and $\mathbf{L_4}$) forms of Fan^{2-} in $\mathbf{3_{Mn}}$ and $\mathbf{3_{Cd}}$ to be investigated by FT-IR spectroscopy (Figure S12). Delocalised C=O stretching, present in both bridging bis-bidentate ($\mathbf{L_1}$ and $\mathbf{L_3}$) and bridging mono- and bi-dentate forms ($\mathbf{L_2}$ and $\mathbf{L_4}$) of Fan^{2-}, is indicated by the strong absorption at 1520 cm^{-1} and weaker shoulder at ca. 1380 cm^{-1}. On the other hand, the strong ν_{C-O} = 1348 cm^{-1} and shoulder at 1035 cm^{-1} is suggestive of the localized C–O bond at the monodentate end of $\mathbf{L_2}$ and $\mathbf{L_4}$. [91-93] Definitive assignment of the intense stretch at 1644 cm^{-1} to uncoordinated, localized C=O of $\mathbf{L_2}$ and $\mathbf{L_4}$ is difficult, as (MeV)Cl$_2$ exhibits a strong absorption in this region, ascribed to aryl $\nu_{C=C}$ stretching.

The crystal packing in the aforementioned ladder-type anionic polymer, (2,2′-bpyH$^+$)$_2$[Mn$_2$(Clan)$_3$(H$_2$O)$_2$]·2H$_2$O, is significantly impacted by extensive H-bond interactions. In $\mathbf{3_{Mn}}$ and $\mathbf{3_{Cd}}$ two types of hydrogen bonding interactions similarly play a major role in dictating crystal packing. These H-bonds extend between coordinated H$_2$O molecules, and O acceptor atoms in $\mathbf{L_2}$ or $\mathbf{L_4}$ ligands in an adjacent 1D ladder chain (Figure 6a). One type of interaction is between a coordinated H$_2$O molecule and an uncoordinated O atom of either $\mathbf{L_2}$ or $\mathbf{L_4}$ ligands in an adjacent ladder ($d_{O\cdots O}$ = 2.669(2) Å and 2.713(2)Å in $\mathbf{3_{Mn}}$; $d_{O\cdots O}$ = 2.702(2) and 2.730(2) Å in $\mathbf{3_{Cd}}$). The other type occurs between the coordinated H$_2$O molecule, and a metal-

coordinated O atom at the bis-bidentate end of $\mathbf{L_2}$ or $\mathbf{L_4}$. A self-complementary interaction from H_2O molecules in the adjacent ladder occurs (Figure 6b), so that the Mn^{II} and coordinated H_2O molecules are situated at diagonally opposite corners of a $Mn_2(H_2O)_2$ parallelogram, when viewed down the ladder axis. These H-bonding interactions occur on both sides of the ladder, forming layers of H-bonded anionic $[M^{II}(Fan)_3(H_2O)_2]^{2-}$ ladders which lie parallel to the crystallographic (1 −1 0) plane. Charge-balancing MeV^{2+} cations, in addition to disordered MeCN and H_2O solvent molecules, reside between the layers of H-bonded layers of anionic $[M^{II}(Fan)_3(H_2O)_2]^{2-}$ ladders, with the central C–C bond of MeV^{2+} oriented approximately parallel to the long axis of the 1D ladders (Figure 7). A modest degree of inter-ring torsion in the MeV^{2+} moieties of 18.2° in $\mathbf{3_{Mn}}$ and 16.1° in $\mathbf{3_{Cd}}$ is apparent. The location of the MeV^{2+} cations in $\mathbf{3_{Mn}}$ and $\mathbf{3_{Cd}}$ contrasts with (2,2′-bpyH)$_2$[Mn_2(Clan)$_3$(H_2O)$_2$]·2H_2O, in which 2,2′-bpyH$^+$ cations partly protrude into the voids of the Mn_4(Clan)$_4$ parallelograms.[48]

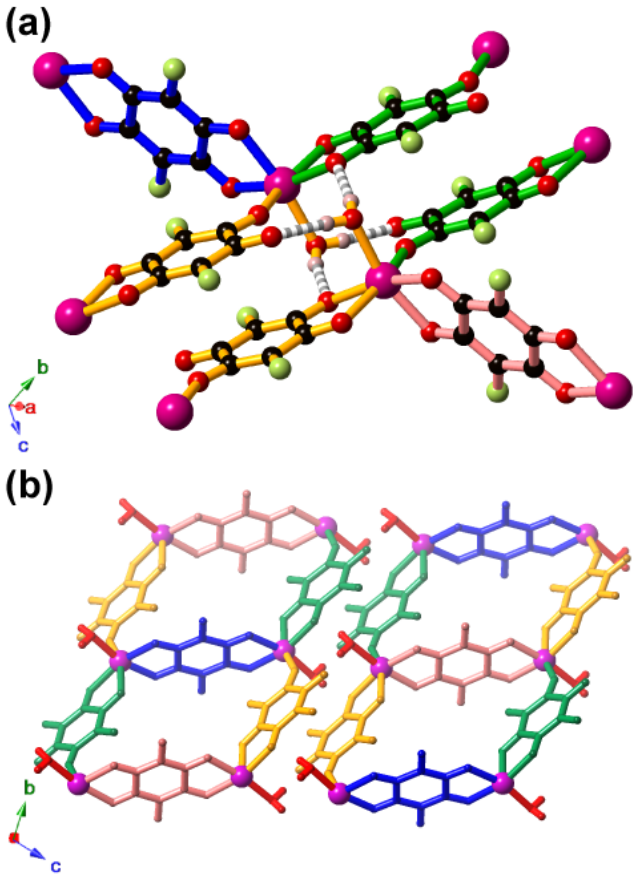

Figure 6. (a) Ball-and-stick representations of the H-bonding (dashed grey) between coordinated H_2O molecules and Fan^{2-} ligands in the 1D $[Mn_2(Fan)_3(H_2O)_2]^{2-}$ ladders. Crystallographically unique ligands $\mathbf{L_1}$ (blue), $\mathbf{L_2}$ (green), $\mathbf{L_3}$ (pink), $\mathbf{L_4}$ (yellow). Magenta = Mn, pale green = F, red = O, black = C, pale pink = H. (b) Ladder-to-ladder packing and symmetry relations of $\mathbf{L_1}$ through $\mathbf{L_4}$ ligands in adjacent anionic ladder facilitated by coordinated H_2O molecules (red).

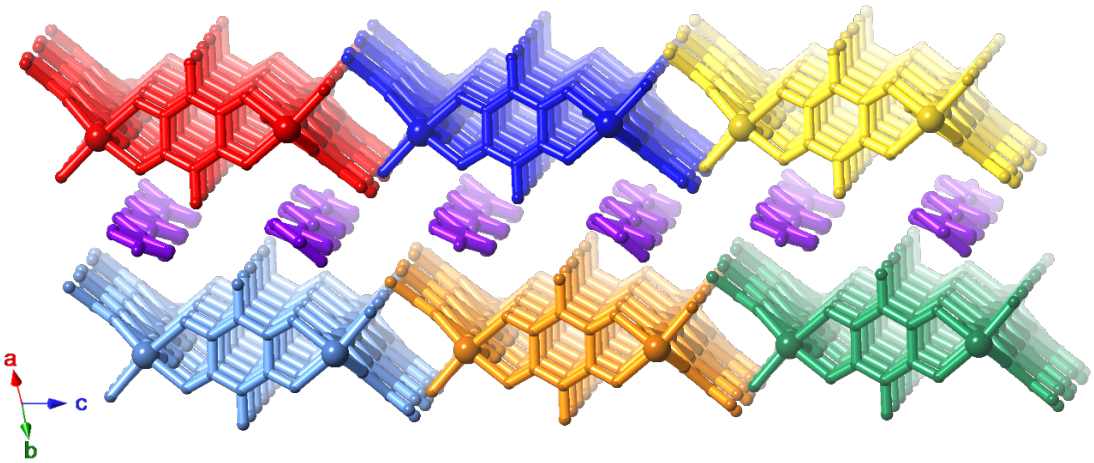

Figure 7. View just off the long axis of the 1D ladders showing packing of MeV^{2+} cations (purple) with the anionic 1D anionic $[M_2(Fan)_3(H_2O)_2]^{2-}$ ladders.

Comparison of the experimental P-XRD patterns between $\mathbf{3}_{\mathbf{Mn}}$ and $\mathbf{3}_{\mathbf{Cd}}$ reveals an interesting contrast. Good agreement is observed between the experimental P-XRD pattern for bulk $\mathbf{3}_{\mathbf{Mn}}$ and the pattern calculated from the SC-XRD structure of $\mathbf{3}_{\mathbf{Mn}}$ (Figure S13), indicating the phase purity of the bulk sample. In contrast, a similar analysis on bulk $\mathbf{3}_{\mathbf{Cd}}$ reveals extraneous peaks which do not match the calculated pattern of $\mathbf{3}_{\mathbf{Cd}}$ (Figure S14), suggesting the presence of a second crystalline phase. Optical microscopy upon the bulk product revealed an inseparable mixture of yellowish-brown plate crystals of the desired $\mathbf{3}_{\mathbf{Cd}}$ phase, in addition to tiny pale-yellow blocks. A structure determination for the second crystalline phase (Table S6), was indicative of a 1D coordination polymer consisting of strips of $[Cd(Fan)(H_2O)_2]$ ($\mathbf{4}_{\mathbf{Cd}}$). Comparison of the experimental P-XRD of bulk $\mathbf{3}_{\mathbf{Cd}}$ with the calculated patterns for $\mathbf{3}_{\mathbf{Cd}}$ and $\mathbf{4}_{\mathbf{Cd}}$ confirms the bulk product contains an inseparable mixture of the $\mathbf{3}_{\mathbf{Cd}}$ and $\mathbf{4}_{\mathbf{Cd}}$ phases. The structure of $\mathbf{4}_{\mathbf{Cd}}$ is essentially isostructural with the 1D strip $[M(dhbq)(H_2O)_2]$ (M = Mg, Mn, Zn) coordination polymers reported earlier,[46, 47] with $\mathbf{4}_{\mathbf{Cd}}$ exhibiting an enlarged unit cell due to the larger van der Waals radius of F compared to H,

leading to large separations between [Cd(Fan)(H_2O)$_2$] strips. The Cd^{II} centers in $\mathbf{4_{Cd}}$ are coordinated by four O donor atoms from bridging bis-bidentate Fan^{2-} ligands, with the remaining *trans* sites occupied by H_2O molecules (Figure S15a). Each coordinated H_2O molecule engages in two H-bonding interactions ($d_{O\cdots O}$ = 2.808 Å) with O acceptors from Fan^{2-} ligands in two adjacent [Cd(Fan)(H_2O)$_2$] strips (Figure S15b). The long axis of the strips and the mean Fan^{2-} planes lie parallel to the crystallographic (–1 0 1), which in combination with the H-bonding interactions between strips, produces a densely packed structure (Figure S15c).

Despite repeated attempts using varying reagent concentrations or stoichiometries, co-crystallization of $\mathbf{4_{Cd}}$ with $\mathbf{3_{Cd}}$ was unavoidable. It is not immediately apparent why an isostructural 1D [Mn(Fan)(H_2O)$_2$] strip does not co-crystallize with $\mathbf{3_{Mn}}$. Recent work by Nielson *et al*. has shown the outcome of reactions targeting anionic Ni–tetraoxolene coordination polymers is impacted by the speed of reagent mixing.[94] Rapid mixing of $^{n}Bu_4NBr$, $Ni(OAc)_2$ and H_2dhbq at either room or elevated temperature yielded only 1D [Ni(dhbq)(H_2O)$_2$] strips, whereas slow addition of $Ni(OAc)_2$ to $^{n}Bu_4NBr$ and H_2dhbq afforded the desired anionic ($^{n}Bu_4N$)$_2$[Ni_2(dhbq)$_3$] coordination polymer. These findings suggest the neutral 1D strip coordination polymers could be favored kinetically at high metal concentration, whereas the anionic metal–tetraoxolene coordination polymers crystallize slower at lower metal concentrations. Unavoidable co-crystallization of $\mathbf{4_{Cd}}$ with $\mathbf{3_{Cd}}$ could therefore occur as $\mathbf{4_{Cd}}$, or the molecular precursor complex, is presumably less soluble than the equivalent Mn^{II} species, so that any $\mathbf{4_{Cd}}$ crystallized cannot transform to $\mathbf{3_{Cd}}$. On the other hand, either [Mn(Fan)(H_2O)$_2$] or the precursor molecular complex are possibly sufficiently soluble to prevent co-crystallization of $\mathbf{3_{Mn}}$ with [Mn(Fan)(H_2O)$_2$].

CONCLUSION

Despite the synthesis of these tetraoxolene coordination polymers under similar conditions, the topologies and geometries of the coordination polymers obtained were largely unexpected. The structural diversity of the compounds suggest that the supramolecular interactions, which guide framework assembly using MeV^{2+} cations, are delicate and are easily perturbed by changes in solvation, or slight differences in the ionic radii or steric volume of the metals and ligands respectively; a summary of weak interactions involving the MeV^{2+} cation is presented in Table S7. The structural variability is perhaps enhanced by the conformational plasticity of the MeV^{2+} as illustrated by torsional angles between 0 and 40° found in this current work. This means that the cation is far from rigid and has the potential to adapt to a variety of cavities that can be formed within anionic polymers.

The structural unpredictability arising from the incorporation of MeV^{2+} cations contrasts with earlier work on fluor- and chloranilate coordination polymers using alkylammonium-based countercations. Using these cations, large isostructural families of compounds were readily obtained regardless of the halogen substituents or metal species. For example, cations such as tetraethylammonium are sandwiched between $M(Xan)_3$ units belonging to parallel (6,3)-networks of composition $[M_2(Xan)_3]^{2-}$ for a variety of metal ions. H-bonding interactions between hydrogen atoms of Et_4N^+ and coordinated O atoms leads to the occupation of a space between sheets that is bounded by six halogen atoms. In this location the cation serves not only to align the 2D networks but also to act as a squat pillar between hexagonal anionic sheets that are ~10 Å apart. The Et_4N^+ cation plays a similar structural role in $[M(Clan)_2]^{2-}$ square grid networks in which the sheets are also ~10 Å apart.[54, 60] Given the clear structure directing role of cations it is not surprising that the strongly contrasting shapes of the cations MeV^{2+} and Et_4N^+ result in very different types of

structures, nevertheless there is some similarity in the way each of these cations interact with anionic metal–tetraoxolene polymers. Within the structures of $\mathbf{1_{Mn}}$, $\mathbf{1_{Cd}}$ and **2a** the interaction of MeV^{2+} hydrogen atoms with coordinated oxygen atoms is a dominant structure-directing influence (Figures 1e and 4d), which is responsible for the geometrical distortion of the diamond networks in $\mathbf{1_{Mn}}$ and $\mathbf{1_{Cd}}$ and the relative positions of adjacent 2D sheets in **2a**. In compounds $\mathbf{3_{Mn}}$ and $\mathbf{3_{Cd}}$, the presence of the coordinated water molecule results in strong O–H···O hydrogen bonding interactions which are anticipated to be much stronger than the interactions the MeV^{2+} cation would be able to make with coordinated fluoranilate O atoms. The MeV^{2+} cation is therefore relegated to the role of an interlayer cation, where its interaction with the anionic polymer is less pronounced than in $\mathbf{1_{Mn}}$, $\mathbf{1_{Cd}}$ and **2a**.

Despite the unpredictable topologies and structural diversity obtained using only one cation, this current investigation further reinforces earlier work that redox-active viologen-like species can successfully act as countercations for anionic tetraoxolene coordination polymers. Given the wide range of viologen species which can be synthesized, there is likely tremendous scope to unearth an even wider variety of structurally and topologically interesting coordination polymers. Future systematic exploration of this space could afford functional tetraoxolene coordination polymers with unique physical properties, arising from their novel topologies and geometries, never previously obtained in these materials.

EXPERIMENTAL SECTION

Synthesis. *Ligands*. 3,6-Difluoro-2,5-dihydroxy-1,4-benzoquinone (fluoranilic acid, H_2Fan) was synthesized via a modified literature[95] procedure from 2,3,5,6-tetrafluoro-1,4-benzoquinone (F_4BQ) which was also obtained via a modified literature procedure.[96] 3,6-Difluoro-1,2,4,5-

tetrahydroxybenzene (H_4Fan) and 3,6-dichloro-1,2,4,5-tetrahydroxybenzene (H_4Clan) were obtained via a modified literature procedure[59] starting from H_2Fan and 3,6-dichloro-2,5-dihydroxy-1,4-benzoquinone (chloranilic acid, H_2Clan) respectively.

*(MeV)[Mn(Clan)$_2$] (**1$_{Mn}$**).* A solution of $Mn^{II}(NO_3)_2{\cdot}4H_2O$ (50.2 mg, 0.2 mmol), $MeV(OTs)_2$ (211.5 mg, 0.4 mmol) and $LiOAc{\cdot}2H_2O$ (26.4 mg, 0.2 mmol) in H_2O (4 mL) was carefully layered below a solution of H_4Clan (63.3 mg, 0.3 mmol) in acetone (10 mL) in a soda glass vial (OD = 25 mm), with a buffer layer of 1:1 v/v acetone/H_2O (4 mL); four diffusion reactions were conducted in parallel. Bright-red elongated octahedra suitable for X-ray diffraction were visible on the vial walls within two days. After 7 days, the crystalline product was isolated by gravimetric separation. The crystalline product was dislodged from the vial walls, and the reaction solutions mixed. The crystalline product was settled, then the turbid mother liquor was removed. The crystalline product was resuspended in 2:1 v/v acetone/H_2O (10 mL) and the products from the parallel reactions combined. The supernatant liquid was decanted, then the crystalline product was washed with fresh 2:1 v/v acetone/H_2O (3 × 50 mL) by resuspension of the crystalline product, sedimentation of the crystalline product and decantation of the supernatant. The crystalline product was then washed with acetone (3 × 50 mL) as above, then isolated by suction filtration (Por. 3 frit), washing with additional acetone (3 × 10 mL), then dried by suction to a free flowing solid to yield **1$_{Mn}$** as a reddish-maroon crystalline powder (119.5 mg, 30.5%). FT-IR (ATR, cm^{-1}): 3051 (w), 1627 (w), 1464 (s), 1379 (w), 1328 (w), 1281 (w), 1263 (w), 1206 (w), 1183(w), 1158(w), 989 (m), 851 (w), 831 (s), 781 (w), 731 (w). Anal. Calcd. for $(C_{12}H_{14}N_2)(Mn_2Cl_4O_8C_{12})$: C, 44.0%; H, 2.15%; N, 4.28%. Found: C, 44.0%; H, 1.51%; N, 4.02%.

*(MeV)[Cd(Clan)$_2$] (**1$_{Cd}$**).* **1$_{Cd}$** was synthesized and isolated analogously to **1$_{Mn}$** using $Cd^{II}(NO_3)_2{\cdot}4H_2O$ (61.7 mg, 0.2 mmol) in place of $Mn^{II}(NO_3)_2{\cdot}4H_2O$; four diffusion reactions were

conducted in parallel. This procedure yielded $\mathbf{1_{Cd}}$ as a bright-red crystalline powder (77.5 mg, 18.1%). FT-IR (ATR, cm^{-1}): 3103 (w), 3050 (w), 1627 (w), 1459 (s), 1326 (w), 1263 (w), 1181 (w), 984 (w), 924 (w), 847 (w), 830 (s), 782 (w), 731 (w). Upon prolonged standing in air, conversion to a partial hydrate occurred. Anal. Calcd. for $(C_{12}H_{14}N_2)(Cd_2Cl_4O_8C_{12})\cdot 0.4H_2O$: C, 40.04%; H, 2.07%; N, 3.89%. Found: C, 40.04%; H, 1.56%; N, 3.84%.

A modified procedure using equivalent volumes of MeCN in place of acetone, additional $Cd^{II}(NO_3)_2\cdot 4H_2O$ (92.5 mg, 0.3 mmol) and $LiOAc\cdot 2H_2O$ (30.6 mg, 0.3 mmol) and with four diffusion reactions conducted in parallel yielded $\mathbf{1_{Cd}}$ as a bright-red crystalline powder (137.8 mg, 32.2%). FT-IR (ATR, cm^{-1}): 3105 (w), 3050 (w), 1627 (w), 1460 (s), 1384 (w), 1326 (w), 1281 (w), 1265 (w), 1205 (w), 1181 (w), 984 (m), 849 (w), 830 (s), 781 (m), 714 (w), 668 (w). Upon prolonged standing in air, conversion to a partial hydrate occurred: Anal. Calcd. for $(C_{12}H_{14}N_2)(Cd_2Cl_4O_8C_{12})\cdot 0.9H_2O$: C, 39.55%; H, 2.19%; N, 3.84%. Found: C, 39.57%; H, 1.82%; N, 3.93%.

*$(MeV)[Mn_2(Clan)_3]\cdot 6MeCN$ (**2a**) and $(MeV)[Mn_2(Clan)_3]\cdot yH_2O$ (**2b**).* A solution of $Mn^{II}(NO_3)_2\cdot 4H_2O$ (75.3 mg, 0.3 mmol), $MeV(OTs)_2$ (211.5 mg, 0.4 mmol) and $LiOAc\cdot 2H_2O$ (30.6 mg, 0.3 mmol) in H_2O (4 mL) was carefully layered below a solution of H_4Clan (63.3 mg, 0.3 mmol) in MeCN (10 mL) in a soda glass vial (OD = 25 mm), with a buffer layer of 1:1 v/v $MeCN/H_2O$ (4 mL). For synthesis of bulk product, four reactions were conducted in parallel. Maroon parallelepiped plates were visible on the vial walls within two days. For **2a**, single crystals were transferred immediately from the mother liquid to a cryoprotective oil; isolation leads to replacement of solvated MeCN with H_2O and conversion to the hydrate $(MeV)[Mn_2(Clan)_3]\cdot yH_2O$ (**2b**). After seven days, the crystalline product was isolated by gravimetric separation similarly as described above for $\mathbf{1_{Mn}}$. The crystalline product from each diffusion reaction was first resuspended

in 2:1 v/v MeCN/H_2O (10 mL) and the separate reaction mixtures combined. The turbid supernatant was then removed, and the crystalline product was washed with 2:1 v/v MeCN/H_2O (3 × 50 mL), then with MeCN (3 × 50 mL). The product was isolated by suction filtration (Por. 3 frit), washed with additional MeCN (3 × 10 mL), then dried by suction to a free-flowing solid yielding **2b** as a maroon powder (137.7 mg, 35.8%). FT-IR (ATR, cm^{-1}): 3416 (br m), 3107 (w), 3052 (w), 1627 (w), 1496 (s), 1460 (s), 1379 (m), 1329 (w), 1280 w), 1219 (w), 1206 (w), 1184 (w), 991 (w), 849 (w), 832 (m), 810 (w), 781 (w), 683 (w). Upon exposure to air, conversion to hydrate solvate occurred: Anal. Calcd. for $(C_{12}H_{14}N_2)(Mn_2Cl_6O_{12}C_{18})\cdot 2.5H_2O$: C, 37.45%; H, 1.99%; N, 2.91%. Found: C, 37.46%; H, 1.66%; N, 2.80%.

*(MeV)[Mn_2(Fan)$_3$(H_2O)$_2$]·y*MeCN·zH_2O (**3$_{Mn}$**)*. A solution of $Mn^{II}(NO_3)_2\cdot 4H_2O$ (75.3 mg, 0.3 mmol), $MeV(OTs)_2$ (211.5 mg, 0.4 mmol) and $LiOAc\cdot 2H_2O$ (30.6 mg, 0.3 mmol) in H_2O (4 mL) was carefully layered below a solution of H_4Fan (53.4 mg, 0.3 mmol) in MeCN (10 mL) in a soda glass vial (OD = 25 mm), with a buffer layer of 1:1 v/v MeCN/H_2O (4 mL). Yellowish-brown plate crystals suitable for X-ray diffraction were visible on the vial walls within two days. After seven days of reaction, the crystalline product was isolated by gravimetric separation similarly as described for **1$_{Mn}$**. The crystalline product was washed with 2:1 v/v MeCN/H_2O (3 × 10 mL) then MeCN (3 × 10 mL). The product was isolated by suction filtration (Por. 3 frit), washed with additional MeCN (3 × 5 mL), then dried by suction to a free-flowing solid, yielding **3$_{Mn}$** as a dark-brown crystalline powder (30.3 mg, 33.0%). FT-IR (ATR, cm^{-1}): 3138 (br m), 2252 (w), 1644 (m), 1520 (s), 1382 (w), 1349 (m), 1276 (w), 1230 (w), 1191 (w), 1079 (w), 1035 (w), 995 (s), 828 (m), 792 (w), 707 (w), 660 (w). Upon exposure to air, partial solvent loss occurred and thus the proposed solvent composition is only tentative and is based upon the C and N analysis: Anal.

Calcd. for $(C_{12}H_{14}N_2)(Mn_2F_6O_{14}C_{18}H_4)\cdot 1.4(C_2H_3N)\cdot 0.4(H_2O)$: C, 42.87%; H, 2.52%; N, 5.18%. Found: C, 42.86%; H, 1.53%; N, 5.19%.

*(MeV)[$Cd_2(Fan)_3(H_2O)_2$]·y$MeCN$·zH_2O (**3**$_{Cd}$) and [$Cd(Fan)(H_2O)_2$] (**4**$_{Cd}$)*. **3**$_{Cd}$ was synthesized and isolated analogously to **3**$_{Mn}$ using $Cd^{II}(NO_3)_2\cdot 4H_2O$ (92.5 mg, 0.3 mmol) in place of $Mn^{II}(NO_3)_2\cdot 4H_2O$, yielding an inseparable mixture of **3**$_{Cd}$ and **4**$_{Cd}$ as a dark-brown crystalline powder (43.3 mg) FT-IR (ATR, cm^{-1}): 3135 (br m), 2253 (w), 1642 (m), 1507 (s), 1382 (w), 1347 (m), 1228 (w), 1190 (w), 1033 (w), 996 (s), 829 (m), 707 (w), 658 (w). Satisfactory analyses could not be obtained as the product contains an inseparable mixture of **3**$_{Cd}$ and **4**$_{Cd}$.

Single Crystal X-ray Diffraction (SC-XRD)

Crystals were transferred directly from the mother liquor into an oil-based cryoprotectant to prevent solvent loss then mounted on nylon loops. Crystallographic data were measured using a Rigaku XtaLAB Synergy-S diffractometer equipped with a graphite monochromated Cu-Kα (λ = 1.54184 Å) microfocus source, a HyPix-6000 E detector, and an Oxford Diffraction Cryostream 800. Data reduction, multi-scan and Gaussian absorption corrections were performed using CrysAlis PRO.[97] For **4**, crystallographic data were collected using the MX2 beamline of the Australian Synchrotron with monochromatic synchrotron radiation (λ = 0.71073 Å) which was fitted with an Oxford Diffraction Cryostream 700.[98] The beamline and endstation equipment was controlled using the Blu-Ice GUI interface,[99] with frame scaling and merging performed using the WebGUI interface autoprocessing routine using XDS and XSCALE.[100] Unit cell indexing and refinement, data reduction and absorption corrections were performed using XDS.[100] Structure solution was performed with SHELXT using intrinsic phasing,[101] then refined using the SHELXL2018 package with least squares minimization on F^2,[102] through the ShelXle[103] and OLEX2[104] graphical user interfaces. Unless otherwise noted, the thermal and positional parameters

for non-hydrogen atoms in the asymmetric unit were refined anisotropically. Hydrogen atoms were placed at calculated positions using suitable riding models and refined using isotropic displacement parameters derived from their parent atoms.

Powder X-ray Diffraction (P-XRD)

For $\mathbf{1}_{\mathbf{Mn}}$, $\mathbf{1}_{\mathbf{Cd}}$, **2a**, $\mathbf{3}_{\mathbf{Mn}}$ and $\mathbf{3}_{\mathbf{Cd}}$, P-XRD data were collected using a Rigaku XtaLAB Synergy-S diffractometer equipped with a graphite monochromated Cu-Kα (λ = 1.54184 Å) microfocus source and a HyPix-6000 E detector. The temperature was controlled using an Oxford Diffraction Cryostream 800, and data processing were performed using CrysAlis PRO.[97] For **2b**, P-XRD data were collected using the PD beamline at the Australian Synchrotron.[105] The experiments were undertaken using monochromatic synchrotron radiation (λ = 0.58835 Å), which was refined against a NIST SRM LaB_6-660c standard using the GSAS-II interface.[106] Data were collected using the Mythen microstrip detector[107] from 2–76.8° (λ = 0.58835 Å) in 2θ, with the sample temperature maintained using an Oxford Cryostream 700. To cover the gaps between detector modules, two datasets were collected with the detector set 0.5° apart and then merged to a single dataset using PDViPeR (https://www.ansto.gov.au/user-access/instruments/australian-synchrotron-beamlines/powder-diffraction/pdviper). For **2a**, the solvated crystalline product was gently ground under MeCN prevent solvent loss, then transferred as an MeCN slurry to a borosilicate capillary (OD = 0.7 mm) before being flame-sealed. For isolated compounds ($\mathbf{1}_{\mathbf{Mn}}$, $\mathbf{1}_{\mathbf{Cd}}$, **2b**, $\mathbf{3}_{\mathbf{Mn}}$ and $\mathbf{3}_{\mathbf{Cd}}$), the crystalline products were ground in air then loaded into borosilicate capillaries (OD = 0.5 mm), being flame-sealed, then measured at 100 K. Indexing of all P-XRD data were performed using CONOGRAPH graphical user interface.[108]

ASSOCIATED CONTENT

Supporting Information. The Supporting Information is available free-of-charge on the ACS Publications website at DOI: xxxxx.

Additional experimental and synthetic details, crystallographic tables and additional details of structure refinement, P-XRD analyses, additional crystal structure figures, FT-IR, TGA and extended discussion and analysis of MeV^{2+} valence state (PDF), details of close MeV^{2+} - anilate contacts

Crystallographic data for reported structures $\mathbf{1}_{Mn}$, $\mathbf{1}_{Cd}$, **2a**, $\mathbf{3}_{Mn}$, $\mathbf{3}_{Cd}$ and $\mathbf{4}_{Cd}$ (CIF)

Accession Codes. CCDC 2119742-2119747 contain the supplementary crystallographic data for this paper, which can be obtained and can be obtained free-of-charge via www.ccdc.cam.ac.uk/conts/retrieving.html (or from the Cambridge Crystallographic Data Center, 12 Union Road, Cambridge CB2 1EZ, U.K.; fax: (+44) 1223-336-033; or deposit@ccdc.cam.ac.uk).

AUTHOR INFORMATION

Corresponding Author

Brendan F. Abrahams – *School of Chemistry, The University of Melbourne, Parkville, Victoria 3010, Australia;* orcid.org/0000-0003-2957-860X; Email: bfa@unimelb.edu.au

Authors

Martin P. van Koeverden – *School of Chemistry, The University of Melbourne, Parkville, Victoria 3010, Australia*; orcid.org/0000-0002-7339-5168

Carol Hua – *School of Chemistry, The University of Melbourne, Parkville, Victoria 3010, Australia*; orcid.org/ 0000-0002-4207-9963

Timothy A. Hudson – *School of Chemistry, The University of Melbourne, Parkville, Victoria 3010, Australia*; orcid.org/000-0002-0343-7756

Richard Robson – *School of Chemistry, The University of Melbourne, Parkville, Victoria 3010, Australia*

Author Contributions

The manuscript was written through contributions of all authors. All authors have given approval to the final version of the manuscript.

Notes

The authors declare no competing financial interest.

ACKNOWLEDGMENTS

The authors gratefully acknowledge the support of the Australian Research Council (DP180101413). This research was undertaken in part using the MX2 beamline at the Australian Synchrotron, part of ANSTO, and made use of the Australian Cancer Research Foundation (ACRF) detector, in addition to the Powder Diffraction beamline at the Australian Synchrotron, part of ANSTO.

REFERENCES

(1) Li, J.-R.; Kuppler, R. J.; Zhou, H.-C., Selective Gas Adsorption and Separation in Metal–Organic Frameworks. *Chem. Soc. Rev.* **2009,** 38, (5), 1477-1504.

(2) Rosi, N. L.; Eckert, J.; Eddaoudi, M.; Vodak, D. T.; Kim, J.; O'Keeffe, M.; Yaghi, O. M., Hydrogen Storage in Microporous Metal-Organic Frameworks. *Science* **2003,** 300, (5622), 1127-1129.

(3) Sumida, K.; Rogow, D. L.; Mason, J. A.; McDonald, T. M.; Bloch, E. D.; Herm, Z. R.; Bae, T.-H.; Long, J. R., Carbon Dioxide Capture in Metal–Organic Frameworks. *Chem. Rev.* **2012,** 112, (2), 724-781.

(4) Bloch, W. M.; Burgun, A.; Coghlan, C. J.; Lee, R.; Coote, M. L.; Doonan, C. J.; Sumby, C. J., Capturing Snapshots of Post-Synthetic Metallation Chemistry in Metal–Organic Frameworks. *Nat. Chem.* **2014,** 6, (10), 906-912.

(5) Wang, Q.; Astruc, D., State of the Art and Prospects in Metal–Organic Framework (MOF)-Based and Mof-Derived Nanocatalysis. *Chem. Rev.* **2020,** 120, (2), 1438-1511.

(6) Campbell, M. G.; Sheberla, D.; Liu, S. F.; Swager, T. M.; Dincă, M., Cu_3(Hexaiminotriphenylene)$_2$: An Electrically Conductive 2D Metal–Organic Framework for Chemiresistive Sensing. *Angew. Chem. Int. Ed.* **2015,** 54, (14), 4349-4352.

(7) Aubrey, M. L.; Kapelewski, M. T.; Melville, J. F.; Oktawiec, J.; Presti, D.; Gagliardi, L.; Long, J. R., Chemiresistive Detection of Gaseous Hydrocarbons and Interrogation of Charge Transport in Cu[Ni(2,3-pyrazinedithiolate)$_2$] by Gas Adsorption. *J. Am. Chem. Soc.* **2019,** 141, (12), 5005-5013.

(8) Stone, K. H.; Stephens, P. W.; McConnell, A. C.; Shurdha, E.; Pokhodnya, K. I.; Miller, J. S., $Mn^{II}(TCNQ)_{3/2}(I_3)_{1/2}$–a 3D Network-Structured Organic-Based Magnet and Comparison to a 2D Analog. *Adv. Mater.* **2010,** 22, (23), 2514-2519.

(9) Pedersen, K. S.; Perlepe, P.; Aubrey, M. L.; Woodruff, D. N.; Reyes-Lillo, S. E.; Reinholdt, A.; Voigt, L.; Li, Z.; Borup, K.; Rouzières, M.; Samohvalov, D.; Wilhelm, F.; Rogalev, A.; Neaton, J. B.; Long, J. R.; Clérac, R., Formation of the Layered Conductive Magnet $CrCl_2(pyrazine)_2$ through Redox-Active Coordination Chemistry. *Nat. Chem.* **2018,** 10, (10), 1056-1061.

(10) Thorarinsdottir, A. E.; Harris, T. D., Metal–Organic Framework Magnets. *Chem. Rev.* **2020,** 120, (16), 8716-8789.

(11) D'Alessandro, D. M.; Kanga, J. R. R.; Caddy, J. S., Towards Conducting Metal-Organic Frameworks. *Aust. J. Chem.* **2011,** 64, (6), 718-722.

(12) Allendorf, M. D.; Schwartzberg, A.; Stavila, V.; Talin, A. A., A Roadmap to Implementing Metal–Organic Frameworks in Electronic Devices: Challenges and Critical Directions. *Chem. Eur. J.* **2011,** 17, (41), 11372-11388.

(13) Xie, L. S.; Skorupskii, G.; Dincă, M., Electrically Conductive Metal–Organic Frameworks. *Chem. Rev.* **2020,** 120, (16), 8536-8580.

(14) Clemente-León, M.; Coronado, E.; Martí-Gastaldo, C.; Romero, F. M., Multifunctionality in Hybrid Magnetic Materials Based on Bimetallic Oxalate Complexes. *Chem. Soc. Rev.* **2011,** 40, (2), 473-497.

(15) Mercuri, M. L.; Congiu, F.; Concas, G.; Sahadevan, S. A., Recent Advances on Anilato-Based Molecular Materials with Magnetic and/or Conducting Properties. *Magnetochemistry* **2017,** 3, (2), 17.

(16) Tamaki, H.; Zhong, Z. J.; Matsumoto, N.; Kida, S.; Koikawa, M.; Achiwa, N.; Hashimoto, Y.; Okawa, H., Design of Metal-Complex Magnets. Syntheses and Magnetic Properties of Mixed-

Metal Assemblies $\{NBu_4[MCr(ox)_3]\}_x$ (NBu_4^+ = Tetra(*N*-butyl)ammonium Ion; ox^{2-} = Oxalate Ion; M = Mn^{2+}, Fe^{2+}, Co^{2+}, Ni^{2+}, Cu^{2+}, Zn^{2+}). *J. Am. Chem. Soc.* **1992,** 114, (18), 6974-6979.

(17) Mathonière, C.; Nuttall, C. J.; Carling, S. G.; Day, P., Ferrimagnetic Mixed-Valency and Mixed-Metal Tris(Oxalato)Iron(III) Compounds: Synthesis, Structure, and Magnetism. *Inorg. Chem.* **1996,** 35, (5), 1201-1206.

(18) Decurtins, S.; Schmalle, H. W.; Schneuwly, P.; Oswald, H. R., Photochemical Synthesis and Structure of a 3-Dimensional Anionic Polymeric Network of an Iron(II) Oxalato Complex with Tris(2,2'-bipyridine)iron(II) Cations. *Inorg. Chem.* **1993,** 32, (10), 1888-1892.

(19) Andrés, R.; Brissard, M.; Gruselle, M.; Train, C.; Vaissermann, J.; Malézieux, B.; Jamet, J.-P.; Verdaguer, M., Rational Design of Three-Dimensional (3D) Optically Active Molecule-Based Magnets: Synthesis, Structure, Optical and Magnetic Properties of $\{[Ru(bpy)_3]^{2+}, ClO_4^-, [Mn^{II}Cr^{III}(ox)_3]^-\}_n$ and $\{[Ru(bpy)_2ppy]^+, [M^{II}Cr^{III}(ox)_3]^-\}_n$, with M^{II} = Mn^{II}, Ni^{II}. X-ray Structure of $\{[\Delta Ru(bpy)_3]^{2+}, ClO_4^-, [\Delta Mn^{II}\Delta Cr^{III}(ox)_3]^-\}_n$ and $\{[\Lambda Ru(bpy)_2ppy]^+, [\Lambda Mn^{II}\Lambda Cr^{III}(ox)_3]^-\}_n$. *Inorg. Chem.* **2001,** 40, (18), 4633-4640.

(20) Coronado, E.; Galán-Mascarós, J. R.; Gómez-García, C. J.; Martínez-Agudo, J. M., Molecule-Based Magnets Formed by Bimetallic Three-Dimensional Oxalate Networks and Chiral Tris(bipyridyl) Complex Cations. The Series $[Z^{II}(bpy)_3][ClO_4][M^{II}Cr^{III}(ox)_3]$ (Z^{II} = Ru, Fe, Co, and Ni; M^{II} = Mn, Fe, Co, Ni, Cu, and Zn; ox = Oxalate Dianion). *Inorg. Chem.* **2001,** 40, (1), 113-120.

(21) Fishman, R. S.; Clemente-León, M.; Coronado, E., Magnetic Compensation and Ordering in the Bimetallic Oxalates: Why Are the 2D and 3D Series So Different? *Inorg. Chem.* **2009,** 48, (7), 3039-3046.

(22) Weiss, A.; Riegler, E.; Robl, C., Polymeric 2,5-Dihydroxy-1,4-benzoquinone Transition Metal Complexes $Na_2(H_2O)_{24}[M_2(C_6H_2O_4)_3]$ (M = Mn^{2+}, Cd^{2+}). *Z. Naturforsch., B: Chem. Sci.* **1986,** 41, (12), 1501.

(23) Robl, C.; Weiss, A., Complexes with Substituted 2,5-Dihydroxy-*p*-benzochinones $AEC_6X_2O_4{\cdot}4H_2O$ AE=Ca^{2+} X=Cl, Br. *Mater. Res. Bull.* **1987,** 22, (4), 497-504.

(24) Robl, C., Complexes with Substituted 2,5-Dihydroxy-P-Benzoquinones: The Inclusion Compounds $[Y(H_2O)_3]_2$ $(C_6Cl_2O_4)_3{\cdot}6.6H_2O$ and $[Y(H_2O)_3]_2$ $(C_6Br_2O_4)_3{\cdot}6H_2O$. *Mater. Res. Bull.* **1987,** 22, (11), 1483-1491.

(25) Kitagawa, S.; Kawata, S., Coordination Compounds of 1,4-Dihydroxybenzoquinone and Its Homologues. Structures and Properties. *Coord. Chem. Rev.* **2002,** 224, (1–2), 11-34.

(26) Kawata, S.; Kitagawa, S.; Kondo, M.; Furuchi, I.; Munakata, M., Two-Dimensional Sheets of Tetragonal Copper(II) Lattices: X-Ray Crystal Structure and Magnetic Properties of $[Cu(C_6O_4Cl_2)(C_4H_4N_2)]_n$. *Angew. Chem. Int. Ed. Engl.* **1994,** 33, (17), 1759-1761.

(27) Abrahams, B. F.; Lu, K. D.; Moubaraki, B.; Murray, K. S.; Robson, R., X-Ray Diffraction and Magnetic Studies on a Series of Isostructural Divalent Metal Chloranilates with Zigzag Polymeric Chain Structures and on a Dinuclear Iron(III) Chloranilate. *J. Chem. Soc., Dalton Trans.* **2000**, (11), 1793-1797.

(28) Abrahams, B. F.; Coleiro, J.; Ha, K.; Hoskins, B. F.; Orchard, S. D.; Robson, R., Dihydroxybenzoquinone and Chloranilic Acid Derivatives of Rare Earth Metals. *J. Chem. Soc., Dalton Trans.* **2002**, (8), 1586-1594.

(29) Dei, A.; Gatteschi, D.; Pardi, L.; Russo, U., Tetraoxolene Radical Stabilization by the Interaction with Transition-Metal Ions. *Inorg. Chem.* **1991,** 30, (12), 2589-2594.

(30) Min, K. S.; DiPasquale, A. G.; Golen, J. A.; Rheingold, A. L.; Miller, J. S., Synthesis, Structure, and Magnetic Properties of Valence Ambiguous Dinuclear Antiferromagnetically Coupled Cobalt and Ferromagnetically Coupled Iron Complexes Containing the Chloranilate(2–) and the Significantly Stronger Coupling Chloranilate(•3–) Radical Trianion. *J. Am. Chem. Soc.* **2007,** 129, (8), 2360-2368.

(31) Guo, D.; McCusker, J. K., Spin Exchange Effects on the Physicochemical Properties of Tetraoxolene-Bridged Bimetallic Complexes. *Inorg. Chem.* **2007,** 46, (8), 3257-3274.

(32) DeGayner, J. A.; Jeon, I.-R.; Sun, L.; Dincă, M.; Harris, T. D., 2D Conductive Iron-Quinoid Magnets Ordering up to T_c = 105 K Via Heterogenous Redox Chemistry. *J. Am. Chem. Soc.* **2017,** 139, (11), 4175-4184.

(33) Jeon, I.-R.; Negru, B.; Van Duyne, R. P.; Harris, T. D., A 2D Semiquinone Radical-Containing Microporous Magnet with Solvent-Induced Switching from T_c = 26 to 80 K. *J. Am. Chem. Soc.* **2015,** 137, (50), 15699-15702.

(34) van Koeverden, M. P.; Abrahams, B. F.; D'Alessandro, D. M.; Doheny, P. W.; Hua, C.; Hudson, T. A.; Jameson, G. N. L.; Murray, K. S.; Phonsri, W.; Robson, R.; Sutton, A. L., Tuning Charge-State Localization in a Semiconductive Iron(III)–Chloranilate Framework Magnet Using a Redox-Active Cation. *Chem. Mater.* **2020,** 32, (17), 7551-7563.

(35) Taniguchi, K.; Chen, J.; Sekine, Y.; Miyasaka, H., Magnetic Phase Switching in a Tetraoxolene-Bridged Honeycomb Ferrimagnet Using a Lithium Ion Battery System. *Chem. Mater.* **2017,** 29, (23), 10053-10059.

(36) Liu, L.; DeGayner, J. A.; Sun, L.; Zee, D. Z.; Harris, T. D., Reversible Redox Switching of Magnetic Order and Electrical Conductivity in a 2D Manganese Benzoquinoid Framework. *Chem. Sci.* **2019,** 10, (17), 4652-4661.

(37) Chen, J.; Taniguchi, K.; Sekine, Y.; Miyasaka, H., Electrochemical Development of Magnetic Long-Range Correlations with $T_c = 128\,\mathrm{K}$ in a Tetraoxolene-Bridged Fe-Based Framework. *J. Magn. Magn. Mater.* **2020,** 494, 165818.

(38) Chen, J.; Sekine, Y.; Komatsumaru, Y.; Hayami, S.; Miyasaka, H., Thermally Induced Valence Tautomeric Transition in a Two-Dimensional Fe-Tetraoxolene Honeycomb Network. *Angew. Chem. Int. Ed.* **2018,** 57, (37), 12043-12047.

(39) DeGayner, J. A.; Wang, K.; Harris, T. D., A Ferric Semiquinoid Single-Chain Magnet Via Thermally-Switchable Metal–Ligand Electron Transfer. *J. Am. Chem. Soc.* **2018,** 140, (21), 6550-6553.

(40) Ziebel, M. E.; Darago, L. E.; Long, J. R., Control of Electronic Structure and Conductivity in Two-Dimensional Metal–Semiquinoid Frameworks of Titanium, Vanadium, and Chromium. *J. Am. Chem. Soc.* **2018,** 140, (8), 3040-3051.

(41) Darago, L. E.; Aubrey, M. L.; Yu, C. J.; Gonzalez, M. I.; Long, J. R., Electronic Conductivity, Ferrimagnetic Ordering, and Reductive Insertion Mediated by Organic Mixed-

Valence in a Ferric Semiquinoid Metal–Organic Framework. *J. Am. Chem. Soc.* **2015,** 137, (50), 15703-15711.

(42) Murase, R.; Commons, C. J.; Hudson, T. A.; Jameson, G. N. L.; Ling, C. D.; Murray, K. S.; Phonsri, W.; Robson, R.; Xia, Q.; Abrahams, B. F.; D'Alessandro, D. M., Effects of Mixed Valency in an Fe-Based Framework: Coexistence of Slow Magnetic Relaxation, Semiconductivity, and Redox Activity. *Inorg. Chem.* **2020,** 59, (6), 3619-3630.

(43) Murase, R.; Abrahams, B. F.; D'Alessandro, D. M.; Davies, C. G.; Hudson, T. A.; Jameson, G. N. L.; Moubaraki, B.; Murray, K. S.; Robson, R.; Sutton, A. L., Mixed Valency in a 3D Semiconducting Iron–Fluoranilate Coordination Polymer. *Inorg. Chem.* **2017,** 56, (15), 9025-9035.

(44) Chen, J.; Sekine, Y.; Okazawa, A.; Sato, H.; Kosaka, W.; Miyasaka, H., Chameleonic Layered Metal–Organic Frameworks with Variable Charge-Ordered States Triggered by Temperature and Guest Molecules. *Chem. Sci.* **2020,** 11, (14), 3610-3618.

(45) Kawata, S.; Kitagawa, S.; Kumagai, H.; Kudo, C.; Kamesaki, H.; Ishiyama, T.; Suzuki, R.; Kondo, M.; Katada, M., Rational Design of a Novel Intercalation System. Layer-Gap Control of Crystalline Coordination Polymers, $\{[Cu(CA)(H_2O)_m](G)\}_n$ ($m = 2$, G = 2,5-Dimethylpyrazine and Phenazine; $m = 1$, G = 1,2,3,4,6,7,8,9-Octahydrophenazine). *Inorg. Chem.* **1996,** 35, (15), 4449-4461.

(46) Morikawa, S.; Yamada, T.; Kitagawa, H., Crystal Structure and Proton Conductivity of a One-Dimensional Coordination Polymer, $\{Mn(DHBQ)(H_2O)_2\}$. *Chem. Lett.* **2009,** 38, (7), 654-655.

(47) Abrahams, B. F.; Dharma, A. D.; Dyett, B.; Hudson, T. A.; Maynard-Casely, H.; Kingsbury, C. J.; McCormick, L. J.; Robson, R.; Sutton, A. L.; White, K. F., An Indirect Generation of 1D M^{II}-2,5-Dihydroxybenzoquinone Coordination Polymers, Their Structural Rearrangements and Generation of Materials with a High Affinity for H_2, CO_2 and CH_4. *Dalton Trans*. **2016,** 45, (4), 1339-1344.

(48) Androš Dubraja, L.; Molčanov, K.; Žilić, D.; Kojić-Prodić, B.; Wenger, E., Multifunctionality and Size of the Chloranilate Ligand Define the Topology of Transition Metal Coordination Polymers. *New J. Chem*. **2017,** 41, (14), 6785-6794.

(49) Kumagai, H.; Kawata, S.; Kitagawa, S., Fabrication of Infinite Two-Dimensional Sheets of Tetragonal Metal(II) Lattices: X-ray Crystal Structures and Magnetic Properties of $[M(CA)(pyz)]_n$ (M^{2+}=Mn^{2+} and Co^{2+}; H_2CA=Chloranilic Acid; pyz=Pyrazine). *Inorg. Chim. Acta* **2002,** 337, 387-392.

(50) Riley, P. E.; Haddad, S. F.; Raymond, K. N., Preparation of Praseodymium(III) Chloranilate and the Crystal Structures of $Pr_2(C_6Cl_2O_4)_3 \cdot 8C_2H_5OH$ and $Na_3[C_6H_2O(OH)(SO_3)_2] \cdot H_2O$. *Inorg. Chem*. **1983,** 22, (21), 3090-3096.

(51) Benmansour, S.; Pérez-Herráez, I.; Cerezo-Navarrete, C.; López-Martínez, G.; Martínez Hernández, C.; Gómez-García, C. J., Solvent-Modulation of the Structure and Dimensionality in Lanthanoid–Anilato Coordination Polymers. *Dalton Trans*. **2018,** 47, (19), 6729-6741.

(52) Bondaruk, K.; Hua, C., Effect of Counterions on the Formation and Structures of Ce(III) and Er(III) Chloranilate Frameworks. *Cryst. Growth Des*. **2019,** 19, (6), 3338-3347.

(53) Ziebel, M. E.; Ondry, J. C.; Long, J. R., Two-Dimensional, Conductive Niobium and Molybdenum Metal–Organic Frameworks. *Chem. Sci.* **2020,** 11, (26), 6690-6700.

(54) Abrahams, B. F.; Grannas, M. J.; Hudson, T. A.; Hughes, S. A.; Pranoto, N. H.; Robson, R., Synthesis, Structure and Host-Guest Properties of $(Et_4N)_2[Sn^{IV}Ca^{II}(chloranilate)_4]$, a New Type of Robust Microporous Coordination Polymer with a 2D Square Grid Structure. *Dalton Trans.* **2011,** 40, (45), 12242-12247.

(55) Luo, T.-T.; Liu, Y.-H.; Tsai, H.-L.; Su, C.-C.; Ueng, C.-H.; Lu, K.-L., A Novel Hybrid Supramolecular Network Assembled from Perfect π– π Stacking of an Anionic Inorganic Layer and a Cationic Hydronium-Ion-Mediated Organic Layer. *Eur. J. Inorg. Chem.* **2004,** 2004, (21), 4253-4258.

(56) Shilov, G. V.; Nikitina, Z. K.; Ovanesyan, N. S.; Aldoshin, S. M.; Makhaev, V. D., Phenazineoxonium Chloranilatomanganate and Chloranilatoferrate: Synthesis, Structure, Magnetic Properties, and Mössbauer Spectra. *Russ. Chem. Bull.* **2011,** 60, (6), 1209-1219.

(57) Benmansour, S.; Abhervé, A.; Gómez-Claramunt, P.; Vallés-García, C.; Gómez-García, C. J., Nanosheets of Two-Dimensional Magnetic and Conducting Fe(II)/Fe(III) Mixed-Valence Metal–Organic Frameworks. *ACS Appl. Mater. Interfaces* **2017,** 9, (31), 26210-26218.

(58) Liu, L.; Li, L.; DeGayner, J. A.; Winegar, P. H.; Fang, Y.; Harris, T. D., Harnessing Structural Dynamics in a 2D Manganese–Benzoquinoid Framework to Dramatically Accelerate Metal Transport in Diffusion-Limited Metal Exchange Reactions. *J. Am. Chem. Soc.* **2018,** 140, (36), 11444-11453.

(59) Kingsbury, C. J.; Abrahams, B. F.; D'Alessandro, D. M.; Hudson, T. A.; Murase, R.; Robson, R.; White, K. F., Role of NEt_4^+ in Orienting and Locking Together $[M_2lig_3]^{2-}$ (6,3) Sheets (H_2lig = Chloranilic or Fluoranilic Acid) to Generate Spacious Channels Perpendicular to the Sheets. *Cryst. Growth Des.* **2017,** 17, (4), 1465-1470.

(60) Kingsbury, C. J.; Abrahams, B. F.; Auckett, J. E.; Chevreau, H.; Dharma, A. D.; Duyker, S.; He, Q.; Hua, C.; Hudson, T. A.; Murray, K. S.; Phonsri, W.; Peterson, V. K.; Robson, R.; White, K. F., Square Grid Metal–Chloranilate Networks as Robust Host Systems for Guest Sorption. *Chem. Eur. J.* **2019,** 25, (20), 5222-5234.

(61) Abrahams, B. F.; Hudson, T. A.; McCormick, L. J.; Robson, R., Coordination Polymers of 2,5-Dihydroxybenzoquinone and Chloranilic Acid with the (10,3)-*a* Topology. *Cryst. Growth Des.* **2011,** 11, (7), 2717-2720.

(62) Nakabayashi, K.; Ohkoshi, S.-i., Monometallic Lanthanoid Assembly Showing Ferromagnetism with a Curie Temperature of 11 K. *Inorg. Chem.* **2009,** 48, (18), 8647-8649.

(63) Benmansour, S.; Vallés-García, C.; Gómez-Claramunt, P.; Mínguez Espallargas, G.; Gómez-García, C. J., 2D and 3D Anilato-Based Heterometallic M(I)M(III) Lattices: The Missing Link. *Inorg. Chem.* **2015,** 54, (11), 5410-5418.

(64) Milašinović, V.; Molčanov, K., Nitranilic Acid as a Basis for Construction of Coordination Polymers: From Discrete Monomers to 3D Networks. *CrystEngComm* **2019,** 21, (18), 2962-2969.

(65) Liang, C.; Zhang, S.; Cheng, L.; Xie, J.; Zhai, F.; He, Y.; Wang, Y.; Chai, Z.; Wang, S., Thermoplastic Membranes Incorporating Semiconductive Metal–Organic Frameworks: An Advance on Flexible X-ray Detectors. *Angew. Chem. Int. Ed.* **2020,** 59, (29), 11856-11860.

(66) Nagayoshi, K.; Kabir, M. K.; Tobita, H.; Honda, K.; Kawahara, M.; Katada, M.; Adachi, K.; Nishikawa, H.; Ikemoto, I.; Kumagai, H.; Hosokoshi, Y.; Inoue, K.; Kitagawa, S.; Kawata, S., Design of Novel Inorganic–Organic Hybrid Materials Based on Iron-Chloranilate Mononuclear Complexes: Characteristics of Hydrogen-Bond-Supported Layers toward the Intercalation of Guests. *J. Am. Chem. Soc.* **2003,** 125, (1), 221-232.

(67) Atzori, M.; Pop, F.; Auban-Senzier, P.; Gómez-García, C. J.; Canadell, E.; Artizzu, F.; Serpe, A.; Deplano, P.; Avarvari, N.; Mercuri, M. L., Structural Diversity and Physical Properties of Paramagnetic Molecular Conductors Based on Bis(Ethylenedithio)Tetrathiafulvalene (BEDT-TTF) and the Tris(chloranilato)ferrate(III) Complex. *Inorg. Chem.* **2014,** 53, (13), 7028-7039.

(68) Atzori, M.; Pop, F.; Auban-Senzier, P.; Clérac, R.; Canadell, E.; Mercuri, M. L.; Avarvari, N., Complete Series of Chiral Paramagnetic Molecular Conductors Based on Tetramethyl-Bis(Ethylenedithio)-Tetrathiafulvalene (TM-BEDT-TTF) and Chloranilate-Bridged Heterobimetallic Honeycomb Layers. *Inorg. Chem.* **2015,** 54, (7), 3643-3653.

(69) Sahadevan, S. A.; Abhervé, A.; Monni, N.; Auban-Senzier, P.; Cano, J.; Lloret, F.; Julve, M.; Cui, H.; Kato, R.; Canadell, E.; Mercuri, M. L.; Avarvari, N., Magnetic Molecular Conductors Based on Bis(Ethylenedithio)Tetrathiafulvalene (BEDT-TTF) and the Tris(chlorocyananilato)ferrate(III) Complex. *Inorg. Chem.* **2019,** 58, (22), 15359-15370.

(70) Sahadevan, S. A.; Abhervé, A.; Monni, N.; Auban-Senzier, P.; Cui, H.; Kato, R.; Mercuri, M. L.; Avarvari, N., Radical Cation Salts of Tetramethyltetrathiafulvalene (TM-TTF) and Tetramethyltetraselenafulvalene (TM-TSF) with Chlorocyananilate-Based Anions. *Cryst. Growth Des.* **2020,** 20, (10), 6777-6786.

(71) Striepe, L.; Baumgartner, T., Viologens and Their Application as Functional Materials. *Chem. Eur. J.* **2017,** 23, (67), 16924-16940.

(72) Mortimer, R. J., Organic Electrochromic Materials. *Electrochim. Acta* **1999,** 44, (18), 2971-2981.

(73) Madasamy, K.; Velayutham, D.; Suryanarayanan, V.; Kathiresan, M.; Ho, K.-C., Viologen-Based Electrochromic Materials and Devices. *J. Mater. Chem. C* **2019,** 7, (16), 4622-4637.

(74) Trabolsi, A.; Khashab, N.; Fahrenbach, A. C.; Friedman, D. C.; Colvin, M. T.; Cotí, K. K.; Benítez, D.; Tkatchouk, E.; Olsen, J.-C.; Belowich, M. E.; Carmielli, R.; Khatib, H. A.; Goddard, W. A.; Wasielewski, M. R.; Stoddart, J. F., Radically Enhanced Molecular Recognition. *Nat. Chem.* **2010,** 2, (1), 42-49.

(75) Sun, J.; Wu, Y.; Wang, Y.; Liu, Z.; Cheng, C.; Hartlieb, K. J.; Wasielewski, M. R.; Stoddart, J. F., An Electrochromic Tristable Molecular Switch. *J. Am. Chem. Soc.* **2015,** 137, (42), 13484-13487.

(76) Hünig, S.; Schenk, W., Two-Step Redox Systems, XXVI - Influence of *N*-Substituents in 4,4′-Bipyridyls on Redox Properties, Stability of Radical Ions and UV-Spectra. *Liebigs Ann. Chem.* **1979,** 1979, (10), 1523-1533.

(77) Bird, C. L.; Kuhn, A. T., Electrochemistry of the Viologens. *Chem. Soc. Rev.* **1981,** 10, (1), 49-82.

(78) Nakahara, A.; Wang, J. H., Charge-Transfer Complexes of Methylviologen. *The Journal of Physical Chemistry* **1963,** 67, (2), 496-498.

(79) Ashton, P. R.; Balzani, V.; Becher, J.; Credi, A.; Fyfe, M. C. T.; Mattersteig, G.; Menzer, S.; Nielsen, M. B.; Raymo, F. M.; Stoddart, J. F.; Venturi, M.; Williams, D. J., A Three-Pole Supramolecular Switch. *J. Am. Chem. Soc.* **1999,** 121, (16), 3951-3957.

(80) Bockman, T. M.; Kochi, J. K., Isolation and Oxidation-Reduction of Methylviologen Cation Radicals. Novel Disproportionation in Charge-Transfer Salts by X-ray Crystallography. *J. Org. Chem.* **1990,** 55, (13), 4127-4135.

(81) Geraskina, M. R.; Dutton, A. S.; Juetten, M. J.; Wood, S. A.; Winter, A. H., The Viologen Cation Radical Pimer: A Case of Dispersion-Driven Bonding. *Angew. Chem. Int. Ed.* **2017,** 56, (32), 9435-9439.

(82) Huang, F.; Switek, K. A.; Zakharov, L. N.; Fronczek, F. R.; Slebodnick, C.; Lam, M.; Golen, J. A.; Bryant, W. S.; Mason, P. E.; Rheingold, A. L.; Ashraf-Khorassani, M.; Gibson, H. W., Bis(*m*-phenylene)-32-Crown-10-Based Cryptands, Powerful Hosts for Paraquat Derivatives. *J. Org. Chem.* **2005,** 70, (8), 3231-3241.

(83) Yang, F.; Deng, J.-C.; Li, Z.-G.; Xu, J.-W., 1,1'-Dimethyl-4,4'-bipyridinium Bis(tetrafluoridoborate). *Acta Crystallogr. E* **2008,** 64, (1), o253.

(84) Leblanc, N.; Mercier, N.; Toma, O.; Kassiba, A. H.; Zorina, L.; Auban-Senzier, P.; Pasquier, C., Unprecedented Stacking of MV^{2+} Dications and $MV^{\bullet+}$ Radical Cations in the Mixed-Valence Viologen Salt $(MV)_2(BF_4)_3$ (MV = Methylviologen). *Chem. Commun.* **2013,** 49, (87), 10272-10274.

(85) Alvarez, S.; Avnir, D.; Llunell, M.; Pinsky, M., Continuous Symmetry Maps and Shape Classification. The Case of Six-Coordinated Metal Compounds. *New J. Chem.* **2002,** 26, (8), 996-1009.

(86) Alvarez, S., Distortion Pathways of Transition Metal Coordination Polyhedra Induced by Chelating Topology. *Chem. Rev.* **2015,** 115, (24), 13447-13483.

(87) Ockwig, N. W.; Delgado-Friedrichs, O.; O'Keeffe, M.; Yaghi, O. M., Reticular Chemistry: Occurrence and Taxonomy of Nets and Grammar for the Design of Frameworks. *Acc. Chem. Res.* **2005,** 38, (3), 176-182.

(88) Alexandrov, E. V.; Blatov, V. A.; Kochetkov, A. V.; Proserpio, D. M., Underlying Nets in Three-Periodic Coordination Polymers: Topology, Taxonomy and Prediction from a Computer-Aided Analysis of the Cambridge Structural Database. *CrystEngComm* **2011,** 13, (12), 3947-3958.

(89) Shevchenko, A. P.; Alexandrov, E. V.; Golov, A. A.; Blatova, O. A.; Duyunova, A. S.; Blatov, V. A., Topology Versus Porosity: What Can Reticular Chemistry Tell Us About Free Space in Metal–Organic Frameworks? *Chem. Commun.* **2020,** 56, (67), 9616-9619.

(90) Gao, H.; Zhang, X.-M., Three Novel Bi(III) Complexes with in Situ Generated Anilate Ligands: Unusual Oxidation of Cyclohexanedione to Dihydroxy Benzoquinone. *Dalton Trans.* **2012,** 41, (5), 1562-1567.

(91) Molčanov, K.; Jurić, M.; Kojić-Prodić, B., Stacking of Metal Chelating Rings with π-Systems in Mononuclear Complexes of Copper(II) with 3,6-Dichloro-2,5-dihydroxy-1,4-benzoquinone (Chloranilic Acid) and 2,2′-Bipyridine Ligands. *Dalton Trans.* **2013,** 42, (44), 15756-15765.

(92) Molčanov, K.; Jurić, M.; Kojić-Prodić, B., A Novel Type of Coordination Mode of Chloranilic Acid Leading to the Formation of Polymeric Coordination Ribbon in the Series of Mixed-Ligand Copper(II) Complexes with 1,10-Phenanthroline. *Dalton Trans*. **2014,** 43, (19), 7208-7218.

(93) Jurić, M.; Molčanov, K.; Žilić, D.; Kojić-Prodić, B., From Mononuclear to Linear One-Dimensional Coordination Species of Copper(II)–Chloranilate: Design and Characterization. *RSC Adv*. **2016,** 6, (67), 62785-62796.

(94) Nielson, K. V.; Zhang, L.; Zhang, Q.; Liu, T. L., A Strategic High Yield Synthesis of 2,5-Dihydroxy-1,4-benzoquinone Based MOFs. *Inorg. Chem*. **2019,** 58, (16), 10756-10760.

(95) Wallenfels, K.; Friedrich, K., Über Fluorchinone, II. Zur Hydrolyse Und Alkoholyse Des Fluoranils. *Chem. Ber*. **1960,** 93, (12), 3070-3082.

(96) Essers, M.; Haufe, G., Chemical Consequences of Fluorine Substitution. Part 4. Diels–Alder Reactions of Fluorinated *p*-Benzoquinones with Dane's Diene. Synthesis of Fluorinated D-Homosteroids. *J. Chem. Soc., Perkin Trans. 1* **2002**, (23), 2719-2728.

(97) Agilent, *CrysAlis Pro*. ed.; Agilent Technologies Ltd: Yarnton, Oxfordshire, England, 2014.

(98) Aragao, D.; Aishima, J.; Cherukuvada, H.; Clarken, R.; Clift, M.; Cowieson, N. P.; Ericsson, D. J.; Gee, C. L.; Macedo, S.; Mudie, N.; Panjikar, S.; Price, J. R.; Riboldi-Tunnicliffe, A.; Rostan, R.; Williamson, R.; Caradoc-Davies, T. T., MX2: A High-Flux Undulator Microfocus Beamline Serving Both the Chemical and Macromolecular Crystallography Communities at the Australian Synchrotron. *J. Synchrotron Rad*. **2018,** 25, (3), 885-891.

(99) McPhillips, T. M.; McPhillips, S. E.; Chiu, H.-J.; Cohen, A. E.; Deacon, A. M.; Ellis, P. J.; Garman, E.; Gonzalez, A.; Sauter, N. K.; Phizackerley, R. P.; Soltis, S. M.; Kuhn, P., Blu-Ice and the Distributed Control System: Software for Data Acquisition and Instrument Control at Macromolecular Crystallography Beamlines. *J. Synchrotron Rad.* **2002,** 9, (6), 401-406.

(100) Kabsch, W., XDS. *Acta Crystallogr. D* **2010,** 66, (2), 125-132.

(101) Sheldrick, G., SHELXT - Integrated Space-Group and Crystal-Structure Determination. *Acta Crystallogr. A* **2015,** 71, (1), 3-8.

(102) Sheldrick, G., Crystal Structure Refinement with SHELXL. *Acta Crystallogr. C* **2015,** 71, (1), 3-8.

(103) Hübschle, C. B.; Sheldrick, G. M.; Dittrich, B., ShelXle: A Qt Graphical User Interface for SHELXL. *J. Appl. Crystallogr.* **2011,** 44, (6), 1281-1284.

(104) Dolomanov, O. V.; Bourhis, L. J.; Gildea, R. J.; Howard, J. A. K.; Puschmann, H., OLEX2: A Complete Structure Solution, Refinement and Analysis Program. *J. Appl. Crystallogr.* **2009,** 42, (2), 339-341.

(105) Wallwork, K. S.; Kennedy, B. J.; Wang, D., The High Resolution Powder Diffraction Beamline for the Australian Synchrotron. *AIP Conference Proceedings* **2007,** 879, (1), 879-882.

(106) Toby, B. H.; Von Dreele, R. B., GSAS-II: The Genesis of a Modern Open-Source All Purpose Crystallography Software Package. *J. Appl. Crystallogr.* **2013,** 46, (2), 544-549.

(107)Schmitt, B.; Brönnimann, C.; Eikenberry, E. F.; Gozzo, F.; Hörmann, C.; Horisberger, R.; Patterson, B., Mythen Detector System. *Nucl. Instrum. Methods Phys. Res. A* **2003,** 501, (1), 267-272.

(108)Oishi-Tomiyasu, R., Robust Powder Auto-Indexing Using Many Peaks. *J. Appl. Crystallogr.* **2014,** 47, (2), 593-598.

For Table of Contents Use Only

Inducing Structural Diversity in Anionic Metal–Tetraoxolene Coordination Polymers Using Templating Methyl Viologen Countercations

Martin P. van Koeverden†, Brendan F. Abrahams*, Carol Hua‡, Timothy A. Hudson, Richard Robson.

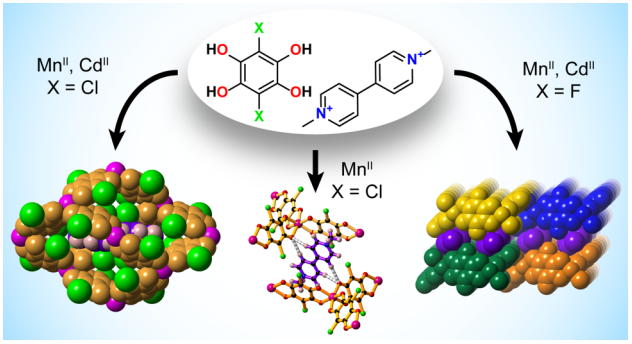

SYNOPSIS

Methyl viologen (MeV^{2+}) acts as a countercation in a range of one-, two- and three-dimensional metal–tetraoxolene coordination polymers. Varying the metal and crystallization solvents alter the non-covalent interactions between MeV^{2+} cations and the anionic tetraoxolene networks, leading to different topologies.